

Accepted For Publication in *The Astrophysical Journal*

Time-dependent Radiation Transfer in the Internal Shock Model Scenario for Blazar Jets

M. Joshi^{1,2} and M. Böttcher¹

*Astrophysical Institute, Department of Physics and Astronomy,
Clippinger Labs, Ohio University, Athens, OH 45701, USA*

*Institute for Astrophysical Research, Boston University,
725 Commonwealth Ave., Boston, MA 02215, USA*

ABSTRACT

We describe the time-dependent radiation transfer in blazar jets, within the internal shock model. We assume that the central engine, which consists of a black hole and an accretion disk, spews out relativistic shells of plasma with different velocity, mass, and energy. We consider a single inelastic collision between a faster (inner) and a slower (outer) moving shell. We study the dynamics of the collision and evaluate the subsequent emission of radiation via the synchrotron and synchrotron self Compton (SSC) processes after the interaction between the two shells has begun. The collision results in the formation of a forward shock (FS) and a reverse shock (RS) that convert the ordered bulk kinetic energy of the shells into magnetic field energy and accelerate the particles, which then radiate. We assume a cylindrical geometry for the emission region of the jet. We treat the self-consistent radiative transfer by taking into account the inhomogeneity in the photon density throughout the region. In this paper, we focus on understanding the effects of varying relevant input parameters on the simulated spectral energy distribution (SED) and spectral variability patterns.

Subject headings: BL Lacertae objects: general — Galaxies: jets — Hydrodynamics — Radiation mechanism: non-thermal — Radiative transfer — Relativistic processes

1. Introduction

Blazars are a class of extreme active galactic nuclei (AGNs). They consist of flat-spectrum radio quasars (FSRQs) and BL Lac objects, and are known for their rapid variability, at all wavelengths, on timescales of months to a few days and even to less than an hour in some cases (e.g., Gaidos et al. 1996; Catanese & Weekes 1999; Aharonian et al. 2007; Albert et al. 2007). Such variability is indicative of highly violent phenomena and the presence of ultra-relativistic particles in the jets of blazars. The SED of blazars consists of two broad spectral bumps that are associated with synchrotron radiation for the low-energy component and inverse Comptonization for the high-energy one. The spectral variability patterns and SEDs provide valuable information regarding the acceleration of particles and the time-dependent interplay of various radiation mechanisms responsible for the observed emission. It is, therefore, imperative to develop a theoretical approach that is capable of simulating these observables to gain a deeper understanding of the physics of blazar jets.

Many authors have studied blazar jets in the past (see, e.g., Maraschi, Ghisellini & Celotti 1992; Dermer & Schlickeiser 1993; Böttcher, Mause & Schlickeiser 1997; Joshi & Böttcher 2007) in the framework of one-zone models. In those works, a spherical emission region has been considered and a power-law energy distribution of injected electrons and positrons assumed. The evolution of the particle population and the subsequent photon emission is solved numerically in a time-dependent manner in order to generate theoretical light curves, spectral variability patterns, SEDs, and other features to obtain a satisfactory fit to the observed data of a given source. Such theoretical efforts have successfully reproduced the observed SED and the spectral variability patterns of various blazars. They have provided information about the relevant physical parameters of the emission region, but the location and the mode of particle acceleration in the jets of such systems still need to be explored in more detail. Most of the theoretical approaches have assumed a spherical geometry for the emission region, continuous injection of particles, and homogeneous population of both electrons and photons throughout the emission region (e.g. Sikora et al. 1994; Bloom & Marscher 1996; Böttcher & Bloom 2000). Such assumptions are good only to a first approximation and do not completely account for the observations. Thus, a more sophisticated approach is required to treat the characteristics of the energized plasma, such as electron energy distribution and magnetic field, not as free parameters but as products of global parameters. This would enable us to link the observed emission properties to the physics of energy transport inside a jet.

In the case of leptonic jet models, various authors have treated the question of particle acceleration and their subsequent injection in different ways. Sokolov et al. (2004) consider the formation of a system of standing oblique shock waves in the jet that accelerate parti-

cles. The local pressure imbalance between the ambient medium and the jet gives rise to standing oblique shock waves, which can terminate in a Mach disk, near the axis, that lies perpendicular to the jet flow. As the relativistic flow of plasma passes through the disk, the plasma electrons accelerate to highly relativistic energies and radiate away their energy via synchrotron and inverse Compton processes to produce the observed emission.

Spada et al. (2001) (hereafter S01) and Mimica et al. (2004), consider the internal shock model to accelerate the particles inside a jet. In this case, shells of plasma with different mass, energy, and velocity are ejected intermittently by the central engine. The faster moving shells catch up with the slower moving ones to result in collisions that produce shocks internal to the jet. These shocks accelerate the plasma electrons to ultrarelativistic energies, which lose their energy via various radiative processes to produce the observed radiation.

All of the above-mentioned approaches consider the formation of reverse and forward shocks that lead to particle acceleration in a region inside the jet. The injection of particles into the emission region continues until the shocks cross the entire region. The population of electrons and photons has been generally approximated to be homogeneous in density throughout the emission region, while the geometry of the region has been assumed to be cylindrical (cubic geometry in case of Chiaberge & Ghisellini (1999)), as appropriate for internal shocks.

Graff et al. (2008) invoke a standing or propagating shock in a collimated jet to accelerate particles. They adopt a multi-zone pipe geometry for the emission region to simulate the resultant radiation and variability of blazars via synchrotron and SSC processes. Their model considers the inhomogeneity in the particle and photon population only in the axial direction when calculating the non-local, time-delayed SSC emission of the source. Their model does not take into account the volume and angle-averaged photon escape timescale for a cylindrical region. Other acceleration scenarios, such as isolated shocks propagating along the jet (Marscher & Gear 1985; Kirk et al. 1998; Sikora et al. 2001), oblique shocks propagating through a pre-existing jet (Ostrowski & Bednarz 2002), or particle acceleration in shear flows (Rieger & Duffy 2004) have also been considered as plausible acceleration mechanisms in blazar jets.

In a recent approach, Böttcher & Dermer (2010) employ the internal shock model to investigate its effects on the time-dependent spectral evolution and cross-frequency correlation of the emission from the jets of blazars. The model considers a one-zone cylindrical emission region bounded by forward and reverse shocks that energize the background plasma to very high energies. The resultant non-thermal distribution of particles then decays in energy through synchrotron, SSC, and external Compton (EC, Compton upscattering of photons external to the jet) emission processes. The time-dependent synchrotron and EC spectra are

calculated analytically, while the SSC emission is computed semi-analytically, with the calculations restricted to the Thomson regime. As a result, their model is unable to reproduce TeV emission from the high-frequency peaked BL Lac objects (HBLs).

In this paper, we consider the internal shock scenario to develop a 1-D multi-slice time-dependent leptonic jet model for simulating the radiative transfer in relativistic blazar jets. We use this scenario to explore the relevant physical parameters of a cylindrical emission region that is responsible for the observed radiation. We take into account the inhomogeneity in the photon and electron populations throughout the region by dividing it into multiple slices and considering time-dependent radiation transfer within and in between each slice. The multi-slice scheme with radiation feedback automatically lets us address the non-local, time-delayed SSC emission of the source in a self-consistent manner along the length of the emission region. It also takes into account the volume and angle-averaged photon escape timescale. We calculate the time-dependent synchrotron and SSC emission spectra without restricting our calculations to the Thomson regime, hence making it applicable to all classes of blazars. We also incorporate the light-travel time delays to correctly calculate the observed spectra and light curves in the observer’s frame. We do not consider the retarded-time photon field individually in the radial direction for calculating the SSC emission neither do we evaluate the microphysics of particle acceleration as that is beyond the scope of the current work.

We assume a background thermal plasma in the jet that contains non-relativistic electrons, positrons, and protons. In §2, we describe the interaction between two shells of plasma, responsible for producing internal shocks, and the subsequent treatment of the collision in the framework of relativistic hydrodynamics. As the shocks propagate through the plasma, the internal kinetic energy of the shocked fluid that is stored in the baryons is transferred to electrons and positrons. This transfer of energy accelerates electrons and positrons to relativistic and non-thermal energies. In this section, we derive various emission region parameters resulting from shock propagation and particle acceleration. In §3, we present a semi-analytical calculation of the volume and angle-averaged photon escape timescale for a cylindrical geometry. In §4, we describe the numerical approach that we use for calculating various radiative energy loss rates as well as photon emissivities. Since positrons lose the same amount of energy as the electrons via the same radiative loss mechanisms, we do not distinguish between them throughout the paper. We discuss our multi-slice radiation transfer scheme that addresses the inhomogeneity in the density of the photon and electron population throughout the emission region. §5 deals with the relevant light-travel time delays that are required to accurately register the radiation in the observer’s frame of reference. The effects of varying the relevant physical input parameters on the simulated SED and lightcurves are discussed in §6. We present our results of the parameter study in §7. We

summarize our results in §8.

Appendices A and B delineate the details of some of the cumbersome equations used in the numerical computation of radiative output. In appendix C, we discuss the numerical approximation used to calculate the synchrotron photon density in the simulations.

2. Hydrodynamics of the collision

In the internal shock scenario, the central engine ejects relativistic shells of plasma with disparate mass and energy that travel with different velocities. As a result, faster moving shells catch up with slower moving ones, released at earlier times, resulting in inelastic collisions. Each collision results in the formation of a FS that propagates into the slower moving outer shell and a RS that propagates into the faster moving inner shell (S01). The shocks are separated by a contact discontinuity (CD) across which the pressure of the shocked fluids is in equilibrium. As the shocks propagate into their respective shells, they convert the ordered bulk kinetic energy of the shocked plasma into magnetic field energy and internal energy of electrons. As a result, electrons are accelerated to highly relativistic energies and radiate to produce the observed emission throughout the electromagnetic spectrum.

In the present paper, we consider a single inelastic collision between a slower moving outer shell and a faster moving inner shell. We study the dynamics of the collision and the subsequent photon emission from non-thermal relativistic electrons after the interaction between the two shells has started. The entire treatment of shell collision and shock propagation is hydrodynamic and relativistic in nature. We do not consider the expansion of individual shells or the merged shell along or transverse to the direction of motion. The respective expansions are neglected here because the jet remains well-collimated at sub-pc and pc scales (Jorstad et al. 2005) and the collision lasts for a short time during which the shell will have a nearly constant width (Böttcher & Dermer 2010).

2.1. Collision parameters

We consider an ejection event of two shells lasting for time t_w . The outer shell is ejected with rest mass M_o , width Δ_o and a bulk Lorentz factor (BLF) Γ_o . The inner shell is ejected with rest mass M_i , width Δ_i and BLF Γ_i . The ejection of the two shells is separated by a time interval t_e . The kinetic luminosity of the entire ejection event is given by L_w such that the sum of the kinetic energies of the two shells is not more than the total specified through L_w and t_w and satisfies the condition:

$$M_o \Gamma_o c^2 + M_i \Gamma_i c^2 = L_w t_w . \quad (1)$$

The radii, R , of both shells are taken to be equal to each other and to that of the collimated jet. The z -axis is along the axis of the jet and the radius of the jet is perpendicular to this axis. At time $t = 0$, the outer shell is at a distance z_o and the inner shell is at a distance z_i from the central engine. In this section, all non-primed quantities refer to the rest frame of the AGN (lab frame), all primed quantities refer to the comoving frame of the shocked fluid behind the shock front, and all quantities with an overline refer to the frame of the unshocked fluid. The time of collision (Kobayashi et al. 1997), δt can then be calculated by

$$\delta t = \frac{(z_o - z_i - \Delta_o)}{c(\beta_i - \beta_o)} \quad (2)$$

and the position at which the two shells would collide, which also defines the location of the CD, is given by

$$z_c = z_i + c\beta_i \delta t . \quad (3)$$

Considering the collision of these two shells to be an inelastic one, the BLF, Γ_m , and the total internal energy of the merged shell, E_{int} , can be obtained by using the conservation of momentum and energy (S01). This yields

$$\Gamma_m = \sqrt{\frac{M_i \Gamma_i + M_o \Gamma_o}{\frac{M_i}{\Gamma_i} + \frac{M_o}{\Gamma_o}}} \quad (4)$$

and

$$E_{\text{int}} = M_i c^2 (\Gamma_i - \Gamma_m) + M_o c^2 (\Gamma_o - \Gamma_m) . \quad (5)$$

The internal energy of both shells before the collision has been assumed to be relatively negligible, so that essentially all of the energy is stored as bulk kinetic energy. The efficiency of conversion of this energy into the internal energy of the merged shell from a single collision is given by

$$\epsilon = 1 - \left[\frac{(M_i + M_o) \Gamma_m}{(M_i \Gamma_i + M_o \Gamma_o)} \right] . \quad (6)$$

In the comoving frame of the shocked (emission) region, the two shocks appear to move in opposite directions, away from the CD, with Lorentz factors $\Gamma'_{\text{fs(rs)}}$, respectively. In the lab frame, the entire shocked material continues to move forward with BLF Γ_{sh} . As a result of shock propagation, the emission region keeps increasing until the shocks reach the respective boundaries of the merged shell, as shown in Figure 1.

The BLF of the entire emission region in the lab frame, Γ_{sh} , is calculated by using the relativistic hydrodynamic Rankine-Hugoniot jump conditions for energy and particle density across both shock fronts, and the condition of equal pressure of the shocked fluids across the CD (S01). The jump equations (Blandford & McKee 1976; Panaitescu & Mészáros 1999) for the kinetic energy density U'_{fs} and the matter density of baryons ρ'_{fs} in the comoving frame of the shocked-fluid frame are given by

$$\frac{U'_{\text{fs(rs)}}}{\rho'_{\text{fs(rs)}}} = c^2 (\Gamma'_{\text{fs(rs)}} - 1) \quad (7)$$

and

$$\frac{\rho'_{\text{fs(rs)}}}{\bar{\rho}_{\text{o(i)}}} = \frac{(\hat{\gamma}\Gamma'_{\text{fs(rs)}} + 1)}{(\hat{\gamma} - 1)}, \quad (8)$$

where $\bar{\rho}_{\text{o(i)}} = \frac{M_{\text{o(i)}}}{\Gamma_{\text{o(i)}} \pi R^2 \Delta_{\text{o(i)}}}$ is the matter baryon density of the preshocked fluid in the comoving frame of the unshocked fluid. The quantity $\hat{\gamma}$ is the adiabatic index, whose value is assumed to be 4/3 (for an ultra-relativistic plasma).

The pressure of the shocked fluids is obtained from equations 7 & 8, and is given by

$$p'_{\text{fs(rs)}} = (\Gamma'_{\text{fs(rs)}} - 1) (\hat{\gamma}\Gamma'_{\text{fs(rs)}} + 1) \bar{\rho}_{\text{o(i)}} c^2. \quad (9)$$

The BLF of each shell relative to the shocked fluids in their respective comoving frames can be written as

$$\Gamma'_{\text{fs(rs)}} = \Gamma_{\text{o(i)}} \Gamma_{\text{sh}} (1 - \beta_{\text{o(i)}} \beta_{\text{sh}}). \quad (10)$$

Substituting Eqn. 10 in Eqn. 9 and applying the condition of equal pressures yields a quartic equation in Γ_{sh}

$$a\Gamma_{\text{sh}}^4 + b\Gamma_{\text{sh}}^3 + c\Gamma_{\text{sh}}^2 + d\Gamma_{\text{sh}} + e = 0. \quad (11)$$

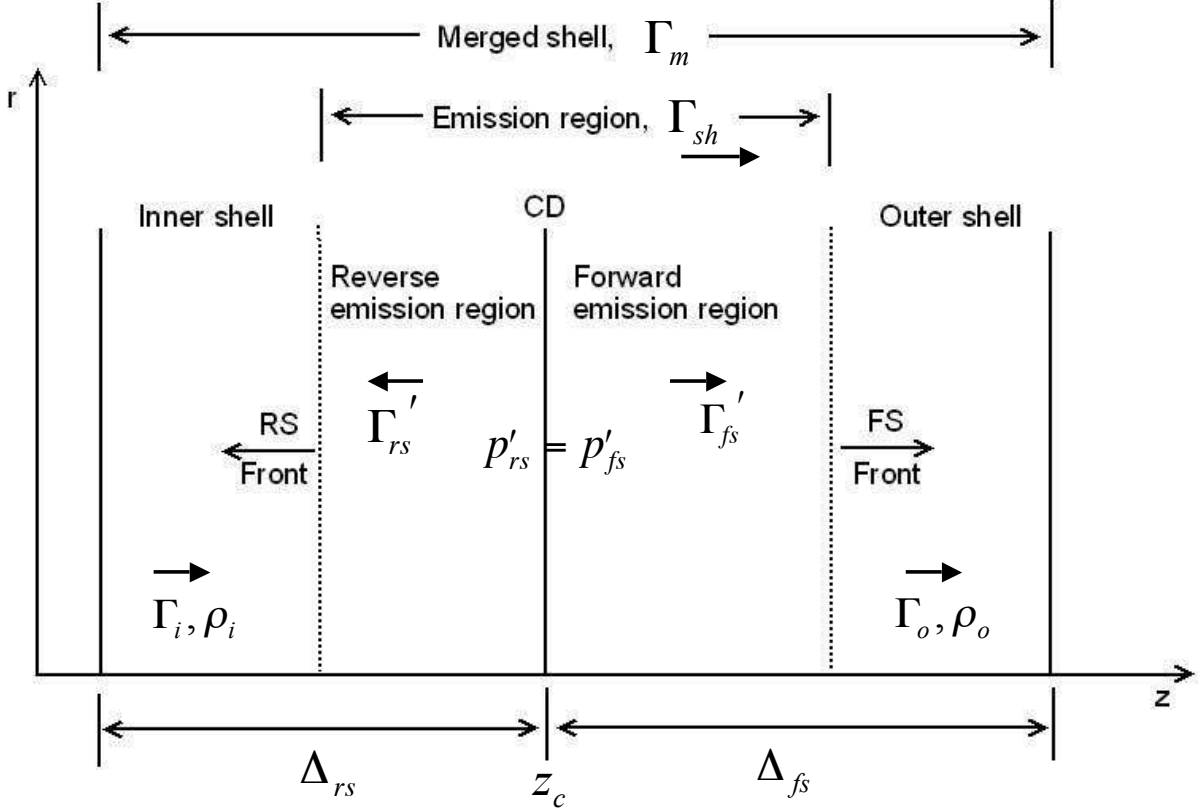


Fig. 1.— Schematic diagram of the two-shell inelastic collision resulting in a merged shell of bulk Lorentz factor (BLF) Γ_m . The forward shock (FS) and reverse shock (RS) fronts start to propagate in the outer and inner shells, respectively, creating the forward and reverse emission regions. In the comoving frame, the shock fronts move with BLFs Γ'_{fs} and Γ'_{rs} . The contact discontinuity (CD) is located at a distance z_c from the central engine. The comoving pressures p'_{fs} and p'_{rs} of the shocked fluids across the CD are equal. Ultra-relativistic electrons are only present in the forward and reverse emission regions. These emission regions keep expanding until the shocks reach the respective boundaries of their regions.

The values of each of these coefficients are given in Appendix A.

As the shocks cross through their respective regions, they compress the plasma present in those regions. As a result, the width of the shocked-fluid region gets compressed. This is determined using the conservation of rest mass of the shocked and unshocked fluids, which is given by

$$\rho'_{\text{fs(rs)}} V'_{\text{fs(rs)}} = \bar{\rho}_{\text{o(i)}} \bar{V}_{\text{o(i)}}. \quad (12)$$

Equation 12 provides the width of the shocked-fluid regions in their respective comoving frames and is given by

$$\Delta'_{\text{fs(rs)}} = \bar{\Delta}_{\text{o(i)}} \left(\frac{\bar{\rho}_{\text{o(i)}}}{\rho'_{\text{fs(rs)}}} \right). \quad (13)$$

The time of crossing the forward or reverse region by the FS or RS, in the shocked-fluid frame, can then be obtained by

$$t'_{\text{cr,fs(rs)}} = \frac{\Delta'_{\text{fs(rs)}}}{c\beta'_{\text{fs(rs)}}}. \quad (14)$$

2.2. Emission Region Parameters

The calculation of the emitted radiation is dependent on the values of the magnetic field (B'), minimum (γ'_{min}) and maximum (γ'_{max}) electron Lorentz factors (ELF), and the normalization factor $Q'_0{}^{\text{inj}}$ ($\text{cm}^{-3}\text{s}^{-1}$) of the electron injection function $Q'_e{}^{\text{inj}}(\gamma, t)$ ($\text{cm}^{-3}\text{s}^{-1}$). The power-law distribution of the injected relativistic electrons is given by

$$Q'_{\text{e,fs(rs)}}{}^{\text{inj}}(\gamma') = Q'_{0,\text{fs(rs)}}{}^{\text{inj}} \gamma'^{-q'} \quad \text{for } \gamma'_{\text{min,fs(rs)}} \leq \gamma' \leq \gamma'_{\text{max,fs(rs)}} \quad (15)$$

where q' is the electron injection power-law index.

In order to proceed with the calculation of emission, we first derive the values of these parameters from shock dynamics (see below) for each of the shocked regions. We calculate the radiative energy loss rates of electrons and corresponding photon emissivities for both regions, separately, and add their respective contributions to the observed spectra.

Some fraction of the bulk kinetic energy density of the shocked fluid is converted into the magnetic and electron energy density by the resulting shocks. We define a magnetic field partition parameter ε'_B such that

$$\varepsilon'_B = \frac{U'_{B,fs(rs)}}{U'_{fs(rs)}} , \quad (16)$$

where $U'_{fs(rs)}$ is the kinetic energy density of the shocked fluid. This is obtained by using Eqns. 7 & 8, and is given by

$$U'_{fs(rs)} = \bar{\rho}_{o(i)} c^2 (\Gamma'_{fs(rs)} - 1) \frac{\hat{\gamma} \Gamma'_{fs(rs)} + 1}{\hat{\gamma} - 1} \quad (17)$$

The quantity $U'_{B,fs(rs)} = B'^2_{fs(rs)}/8\pi$ is the magnetic energy density. Equation 16 yields the value of the magnetic field, which is assumed to be randomly oriented in space and tangled in the jet plasma. The maximum ELF of the injected electrons is obtained by balancing the power gained from the acceleration, i.e. from gyro-resonant processes, with the synchrotron losses (deJager & Harding 1992; Chiang & Dermer 1999). This condition yields

$$\gamma'_{\max,fs(rs)} = 4.6 \times 10^7 \sqrt{\frac{\alpha'}{B'_{fs(rs)}}} , \quad (18)$$

where $\alpha' \leq 1$ is the electron acceleration rate parameter, defined through $\alpha' = t'_{\text{gyr}}/t'_{\text{acc}}$. The quantities t'_{gyr} and t'_{acc} are, respectively, the gyration and acceleration timescales of an electron. The quantity $B'_{fs(rs)}$ is in units of Gauss.

The minimum ELF is obtained by using the equation

$$U'_{e,fs(rs)} = \varepsilon'_e U'_{fs(rs)} . \quad (19)$$

Here, $U'_{e,fs(rs)} = n'_{e,fs(rs)} \langle \gamma'_{fs(rs)} \rangle m_e c^2$ is the electron energy density, $n'_{e,fs(rs)} = \zeta'_e \frac{\rho'_{fs(rs)}}{m_p}$ is the number density of non-thermal electrons injected by shocks into their respective emission regions, ζ'_e is the fraction of electrons that is accelerated behind the shock fronts into the power-law distribution given by Eqn. 15, and ε'_e is the electron energy partition parameter. The average electron energy $\langle \gamma'_{fs(rs)} \rangle$ for the energy range $\gamma'_{\min,fs(rs)} < \gamma'_{fs(rs)} < \gamma'_{\max,fs(rs)}$ is given by

$$\langle \gamma'_{\text{fs(rs)}} \rangle = \frac{\int_{\gamma'_{\text{min,fs(rs)}}}^{\gamma'_{\text{max,fs(rs)}}} n'_{\text{e,fs(rs)}}(\gamma'_{\text{fs(rs)}}) \gamma'_{\text{fs(rs)}} d\gamma'_{\text{fs(rs)}}}{\int_{\gamma'_{\text{min,fs(rs)}}}^{\gamma'_{\text{max,fs(rs)}}} n'_{\text{e,fs(rs)}}(\gamma'_{\text{fs(rs)}}) d\gamma'_{\text{fs(rs)}}} . \quad (20)$$

Here $n'_{\text{e,fs(rs)}}(\gamma'_{\text{fs(rs)}}) = n'_o \gamma'^{-q}_{\text{fs(rs)}}$ is the number density per unit $\gamma'_{\text{fs(rs)}}$ and n'_o is the initial electron number density. As most of the internal kinetic energy of the shocked fluid is stored in the baryons, implying that $\varepsilon'_e \ll 1$, we can write $U'_{\text{fs(rs)}} = n'_{\text{p,fs(rs)}}(\Gamma'_{\text{fs(rs)}} - 1)m_{\text{p}}c^2$. Substituting all of the above expressions along with equation 18 into equation 19, we obtain the following expressions for $\gamma'_{\text{min,fs(rs)}}$:

$$\begin{aligned} C \ln(\gamma'_{\text{min,fs(rs)}}) - \gamma'_{\text{min,fs(rs)}} + \gamma'_{\text{max,fs(rs)}} - C \ln(\gamma'_{\text{max,fs(rs)}}) &= 0 \quad \text{if } q' = 1 \\ \ln(\gamma'_{\text{min,fs(rs)}}) + \frac{C}{\gamma'_{\text{min,fs(rs)}}} - \ln(\gamma'_{\text{max,fs(rs)}}) - \frac{C}{\gamma'_{\text{max,fs(rs)}}} &= 0 \quad \text{if } q' = 2 \\ \gamma'^{(1-q')}_{\text{min,fs(rs)}}(\gamma'_{\text{min,fs(rs)}} - C_q) - \gamma'^{(1-q')}_{\text{max,fs(rs)}}(\gamma'_{\text{max,fs(rs)}} - C_q) &= 0 \quad \text{if } q' \neq 1 \text{ or } 2 , \end{aligned} \quad (21)$$

where $C = 1837 \frac{\varepsilon'_e}{\zeta'_e}(\Gamma'_{\text{fs(rs)}} - 1)$, and $C_q = 1837 \frac{q'-2}{q'-1} \frac{\varepsilon'_e}{\zeta'_e}(\Gamma'_{\text{fs(rs)}} - 1)$. Equation 21 is solved numerically to obtain the value of $\gamma'_{\text{min,fs(rs)}}$. In the case of $\gamma'_{\text{max}} \gg \gamma'_{\text{min}}$ and $q' > 2$, the above expressions reduce to

$$\gamma'_{\text{min,fs(rs)}} = 1837 \frac{q' - 2}{q' - 1} \frac{\varepsilon'_e}{\zeta'_e}(\Gamma'_{\text{fs(rs)}} - 1) . \quad (22)$$

The value of $Q'^{\text{inj}}_{0,\text{fs(rs)}}(t')$ is obtained by assuming that a fraction of the kinetic energy stored in the shocked plasma is transferred, per unit time, to non-thermal electrons (Böttcher & Dermer 2010). This yields

$$\frac{\varepsilon'_e U'_{\text{fs(rs)}}}{t'_{\text{cr,fs(rs)}}} = \int_{\gamma'_{\text{min,fs(rs)}}}^{\gamma'_{\text{max,fs(rs)}}} Q'^{\text{inj}}_{\text{e,fs(rs)}}(\gamma'_{\text{fs(rs)}}, t') \gamma'_{\text{fs(rs)}} m_{\text{e}} c^2 d\gamma'_{\text{fs(rs)}} . \quad (23)$$

Using Eqns. 23 and 15, we obtain the expression for $Q'^{\text{inj}}_{0,\text{fs(rs)}}(t')$ as

$$Q'^{\text{inj}}_{0,\text{fs(rs)}}(t') = \begin{cases} \frac{\varepsilon'_e U'_{\text{fs(rs)}}(2-q')}{m_{\text{e}} c^2 t'_{\text{cr,fs(rs)}} (\gamma'^{(2-q')}_{\text{max,fs(rs)}} - \gamma'^{(2-q')}_{\text{min,fs(rs)}})} & \text{if } q' \neq 2 \\ \frac{\varepsilon'_e U'_{\text{fs(rs)}}}{m_{\text{e}} c^2 t'_{\text{cr,fs(rs)}} \ln(\gamma'_{\text{max,fs(rs)}}/\gamma'_{\text{min,fs(rs)}})} & \text{if } q' = 2 . \end{cases} \quad (24)$$

3. Photon Escape Timescale

For a cylindrical geometry, the volume and angle-averaged photon escape timescale is not the same as that of a spherical one. The average photon escape timescale is used in the numerical computation of the evolution of the particle and photon population inside the emission region. Here, we derive a semi-analytical expression of the escape timescale and assume the cylindrical emission region to be Compton thin.

We consider three possible directions by which a photon can escape from a cylindrical region: forward, sideways and backward. All quantities in this section and thereafter refer to the comoving frame only, unless otherwise indicated, hence the prime notation is no longer used.

Figure 2 depicts the angle considerations for the three possible directions of escape for a photon from a cylindrical region of height (width) h and radius R . As stated earlier, the z -axis is along the axis of the cylinder. The volume-averaged photon escape timescale can then be written as

$$\langle t_{\text{ph,esc}} \rangle_V = \frac{1}{V_{\text{cyl}}} \int_0^R \int_0^h \int_0^{2\pi} \langle t_{\text{ph,esc}}(r, z) \rangle r d\phi dz dr, \quad (25)$$

where the angle-averaged escape timescale is written as

$$\langle t_{\text{ph,esc}}(r, z) \rangle = \frac{1}{4\pi c} \int_0^{2\pi} \int_{-1}^{+1} l_{\text{esc}}(\mu, \Phi; r, z) d\mu d\Phi \quad (26)$$

Here, l_{esc} is the distance required to escape from the region in any direction, and $\mu = \cos \theta$. We have solved the above integral semi-analytically to obtain the final expression for the volume and angle-averaged photon escape timescale for a cylindrical region, which is given in Eqn. 27. The intermediate steps needed to obtain the final expression are given in Appendix B of this paper.

$$\begin{aligned} \langle t_{\text{ph,esc,V}} \rangle = & \frac{h}{4c} - \frac{h}{2c} \ln(a) + \frac{h}{2\pi c} \int_0^{2\pi} \int_0^1 \int_0^1 xy \ln(k^2 + (ay)^2) dy dx d\phi + \\ & \frac{R}{\pi c} \int_0^{2\pi} \int_0^1 xk \arcsin\left(\frac{a}{\sqrt{k^2 + a^2}}\right) dx d\phi - \end{aligned}$$

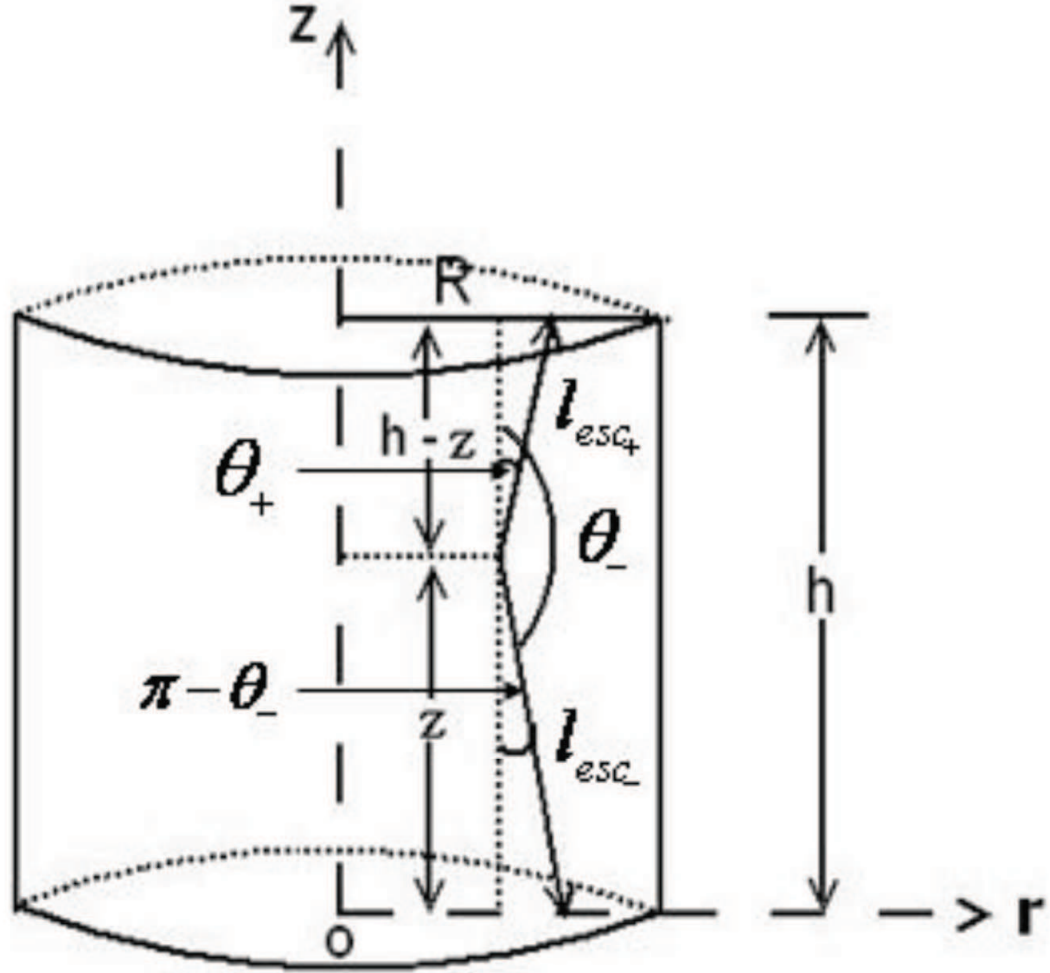


Fig. 2.— Illustration of the three possible directions of escape for a photon from a cylindrical region. The quantities l_{esc+} and l_{esc-} , respectively, refer to the escape path lengths for a photon in forward and backward directions, and θ_+ and $\pi - \theta_-$ are the corresponding angles.

$$\frac{R^2}{2\pi hc} \int_0^{2\pi} \int_0^1 x k^2 \ln \left(1 + \frac{a^2}{k^2} \right) dx d\phi, \quad (27)$$

where $a = h/R$ and $k = \sqrt{1 - (x \sin \phi)^2} - x \cos \phi$.

Using the geometry of a cylinder, the volume-averaged probability of escape for a photon in the forward direction is $P_{\text{fwd}} = \pi R^2 / (2\pi R(R + h))$. The volume-averaged probability for a photon to go in the backward direction is the same as its counterpart in the forward direction, hence $P_{\text{back}} = P_{\text{fwd}}$. Similarly, the volume-averaged probability of escape in the sideways direction is $P_{\text{side}} = 2\pi R h / (2\pi R(R + h)) = h / (R + h)$. These probabilities have been used to calculate the appropriate volume-averaged photon escape rates in the three directions, as described in the next section.

4. Numerical Method

The emission region parameters and the average photon escape timescale form the necessary set of quantities required to calculate radiative energy loss rates and photon emissivities. They are needed to follow the evolution of electron and photon populations inside the emission region in a self-consistent and time-dependent manner along the length of the region. Since the same set of equations is applicable to both the forward and reverse emission regions, we do not distinguish between the various quantities used in the equations.

We consider instantaneous acceleration of relativistic particles behind the shock front. The accelerated particles are injected into the region with a single-power-law distribution described by Eqn. 15. The acceleration of particles and the longitudinal expansion of the emission region continues until the shocks reach their respective boundaries of the merged shell. As the shocks propagate in their region, energetic electrons continue to be produced at the shock front. Owing to energy losses, only less energetic electrons will be found at progressively larger distances from the shock fronts. This creates an energy gradient within the emission region.

Once the acceleration sets in, particles begin to lose their energy via synchrotron and SSC processes. The time-dependent evolution of the electron and photon populations, in each of the emission regions, is followed by using the equations

$$\frac{\partial n_e(\gamma, t)}{\partial t} = -\frac{\partial}{\partial \gamma} \left[\left(\frac{d\gamma}{dt} \right)_{\text{loss}} n_e(\gamma, t) \right] + Q_e(\gamma, t) - \frac{n_e(\gamma, t)}{t_{e, \text{esc}}} \quad (28)$$

and

$$\frac{\partial n_{ph}(\epsilon, t)}{\partial t} = \dot{n}_{ph,em}(\epsilon, t) - \dot{n}_{ph,abs}(\epsilon, t) - \frac{n_{ph}(\epsilon, t)}{t_{ph,esc}}. \quad (29)$$

Here, $(d\gamma/dt)_{\text{loss}}$ is the electron energy loss rate, due to synchrotron and SSC emission, $Q_e(\gamma, t)$ is the sum of external injection and intrinsic $\gamma - \gamma$ pair production rate, and $t_{e,esc} = \eta R/c$ is the electron escape time scale with η being the escape parameter. The quantities $\dot{n}_{ph,em}(\epsilon, t)$ and $\dot{n}_{ph,abs}(\epsilon, t)$ are the photon emission and absorption rates corresponding, respectively, to the electrons' radiative losses and gains, $\epsilon = h\nu/m_e c^2$ is the dimensionless photon energy, and $t_{ph,esc}$ is the volume and angle-averaged photon escape timescale for a cylindrical emission region (Eqn. 27). In order to obtain the temporal evolution of the electron distribution in an emission region, equation 28 is discretized and rearranged in such a way that it forms a tridiagonal matrix, which is then solved numerically (Chiaberge & Ghisellini 1999; Press et al. 1992).

Our current approach simulates the early phase of γ -ray production. During this phase, the radiative cooling dominates over the adiabatic cooling and the emission region remains optically thick out to \lesssim GHz radio frequencies. As a result, the simulated radio flux is well below the observed radio data. We do not model the phase in which the jet components gradually become transparent to radio frequencies because that would introduce several additional and poorly constrained parameters.

The synchrotron loss rate is calculated from (Rybicki & Lightman 1979)

$$\dot{\gamma}_{\text{syn}} = -(4/3)c\sigma_T \frac{B^2 \gamma^2}{8\pi m_e c^2}, \quad (30)$$

where $\sigma_T = 6.65 \times 10^{-25} \text{ cm}^2$ is the Thomson cross-section, and B is obtained from Eqn. 16. The synchrotron photon production rate per unit volume in the energy interval $[\epsilon, \epsilon + d\epsilon]$ is calculated using the formula (Crusius & Schlickeiser 1986)

$$\dot{n}_{\text{syn}}(\epsilon) = \frac{\sqrt{3}e^3 B}{2\pi h^2 \nu} \int_1^\infty R(x) n_e(\gamma) d\gamma, \quad (31)$$

where $x = \frac{4\pi m_e c \nu}{3e B \gamma^2}$. A numerically simplified version of the synchrotron emissivity (described in Appendix C) has been used in our simulations to save CPU time.

We have incorporated the effects of SSA on the synchrotron spectrum in our calculation. The SSA optical depth is calculated using the formula (Rybicki & Lightman 1979)

$$\tau_{\text{SSA}} = \frac{-l_{\text{ph,esc}}\sqrt{3}e^3B}{16\pi^2(m_e c\nu)^2} \int_1^\infty R(x)\gamma^2 \frac{d}{d\gamma}\left(\frac{n_e(\gamma)}{\gamma^2}\right)d\gamma, \quad (32)$$

where $l_{\text{ph,esc}} = t_{\text{ph,esc}} c$ is the mean path length traversed by a photon escaping from its point of origin inside a cylindrical region. The synchrotron emission from a cylindrical region is then obtained using the expression

$$\dot{N}_{\text{syn}}^{\text{esc}}(\epsilon) = \dot{n}_{\text{syn}}(\epsilon) \frac{(1 - \exp(-\tau_{\text{SSA}}))}{\tau_{\text{SSA}}} \pi R^2 h. \quad (33)$$

The electron energy loss rate due to scattering an isotropic, monochromatic radiation field of photon energy ϵ and density n_{ph} (cm^{-3}), including the effects of the Klein-Nishina scattering cross section, is calculated using equation 32 of Böttcher, Mause & Schlickeiser (1997). The photon production rate per unit volume of isotropic SSC emission in the region is calculated by (Jones 1968; Böttcher, Mause & Schlickeiser 1997)

$$\dot{n}_{\text{SSC}}(\epsilon_s, \Omega_s) = \frac{1}{4\pi} \int_1^\infty d\gamma n_e(\gamma) \int_0^\infty d\epsilon n_{\text{ph}}(\epsilon) g(\epsilon_s, \epsilon, \gamma), \quad (34)$$

where ϵ_s is the energy of the scattered photon, and $n_{\text{ph}}(\epsilon)$ is the radiation field at photon energy ϵ available for SSC scattering in the region. The quantity $g(\epsilon_s, \epsilon, \gamma)$ is a function that describes the probability of Compton scattering, and is given by (Jones 1968)

$$g(\epsilon_s, \epsilon, \gamma) = \begin{cases} \frac{3c\sigma_T}{16\gamma^4\epsilon} \left(\frac{4\gamma^2\epsilon_s}{\epsilon} - 1 \right) & \text{for } \frac{\epsilon}{4\gamma^2} \leq \epsilon_s \leq \epsilon \\ \frac{3c\sigma_T}{4\gamma^2\epsilon} \left[2q \ln(q) + (1 + 2q)(1 - q) + \frac{(4\epsilon\gamma q)^2(1-q)}{2(1+4\epsilon\gamma q)} \right] & \text{for } \epsilon \leq \epsilon_s \leq \frac{4\epsilon\gamma^2}{1+4\epsilon\gamma} \end{cases}, \quad (35)$$

where $q = \epsilon_s/4\epsilon\gamma^2(1 - \epsilon_s/\gamma)$. The radiation field available for SSC scattering includes all contributions from the photon field of the previous time step. This accounts for SSC scattering to arbitrarily higher orders. The optical depth for a γ -ray photon of energy ϵ_1 due to $\gamma - \gamma$ absorption is calculated using the formula (Böttcher, Mause & Schlickeiser 1997)

$$\tau_{\gamma\gamma}(\epsilon_1) = 2\pi l_{\text{ph,esc}} \int_{-1}^{+1} d\mu (1 - \mu) \int_{\frac{2}{\epsilon_1(1-\mu)}}^\infty d\epsilon \sigma_{\gamma\gamma}(\epsilon_1, \epsilon, \mu) n_{\text{ph}}(\epsilon, \Omega), \quad (36)$$

where n_{ph} is the photon density present in the emission region that provides the photon field for $\gamma - \gamma$ absorption, and $\sigma_{\gamma\gamma}$ is the pair production cross-section. The subsequent pair production rate is obtained using the exact and analytic solution, given in Eqn. (26) of Böttcher & Schlickeiser (1997). The contribution from pair production is added to Eqn. (28) at every time step of the simulation. Using the radiative transfer equation, the high-energy emission that is able to escape from the region can be calculated as

$$\dot{N}_{\text{SSC}}^{\text{esc}}(\epsilon_s, \Omega_s) = \dot{n}_{\text{SSC}}(\epsilon_s, \Omega_s) \frac{(1 - \exp(-\tau_{\gamma\gamma}))}{\tau_{\gamma\gamma}} \pi R^2 h . \quad (37)$$

The temporal evolution of the photon population inside the emission region, for synchrotron and SSC emission, is followed using equation 29. The time step used in the simulations is a fraction of the minimum time scale among the relevant ones (cooling, electron and photon escape, injection, and shock crossing for as long as the shocks are in the region) from both regions. The simulation time step is taken to be common for both emission regions.

4.1. The Slice Scheme

In order to reproduce the observed spectral variability patterns of a blazar, it is important to consider the inhomogeneity in the particle as well as photon density throughout the emission region. Observations in the optical and higher energy bands indicate that the acceleration and/or cooling timescales can be shorter than the light crossing time for the region (Chiaberge & Ghisellini 1999). The highly energetic electrons that have been accelerated freshly at the shock front evolve on a cooling timescale shorter than the light crossing time, farther from the shock front those ultra-high energy electrons have had time to cool significantly. This induces an energy gradient in the electron population within the region and creates an inhomogeneity in the particle as well as photon energy density throughout the emission region. As a result, the observer sees a combination of various spectra being produced in different parts of the region (see also Sokolov et al. 2004; Graff et al. 2008).

In our model, we have incorporated the inhomogeneity in the particle and photon energy densities by dividing both emission regions into multiple slices, each of width h_z and radius R . As shown in Figure 3, for simplicity we start with a jet that is devoid of relativistic particles. The first population of ultrarelativistic particles is injected by the shocks very close to the CD.

The slice closest to the CD in the forward (reverse) emission region will have the forward (reverse) shock propagating through it first. As the shock advances, it injects particles into the slice with a power-law distribution that is dictated by the shock parameters. The

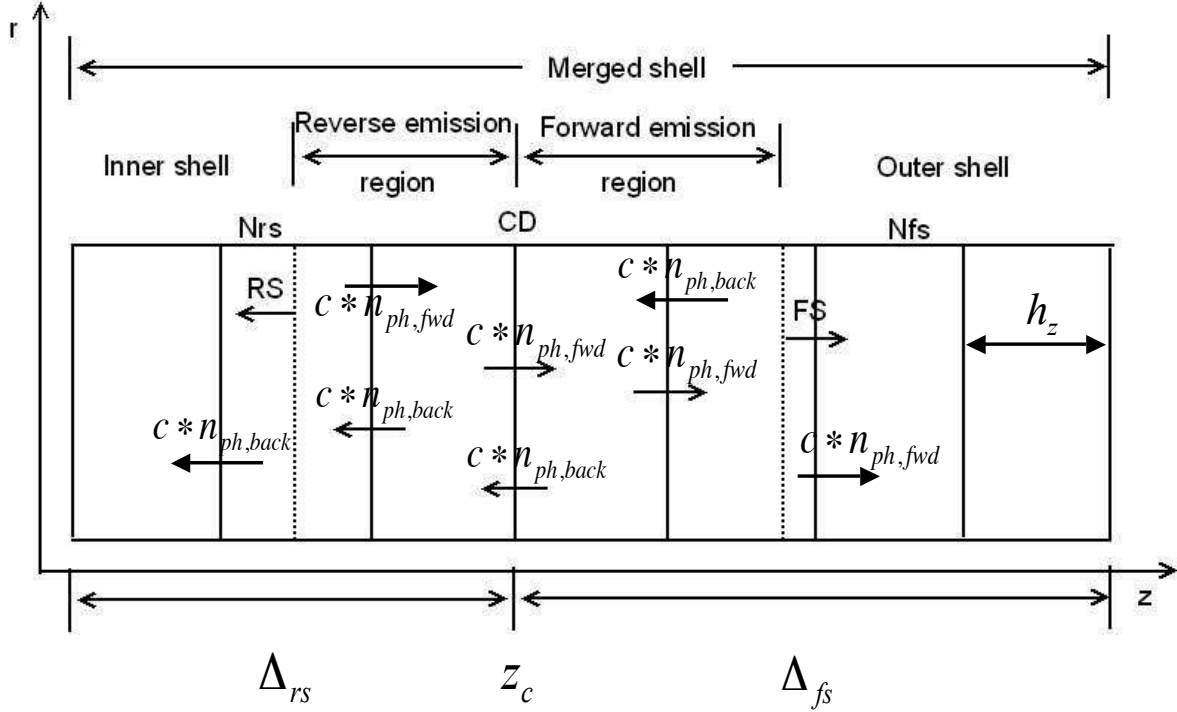


Fig. 3.— Illustration of the slice scheme used to calculate the integrated radiation spectrum resulting from the emission regions shown in Fig. 1. The entire forward and reverse emission regions are divided into N_{fs} and N_{rs} slices, each of width h_z . The quantities $c \times n_{ph,fwd}$, $c \times n_{ph,back}$, and $c \times n_{ph,side}$ are the photon fluxes (photons per unit time per unit area of the slice) in the forward, backward, and sideways directions delineating the transfer of photons in between the slices throughout the forward and reverse emission regions.

normalization factor, Q_0^{inj} is calculated for every slice using equation 24 and replacing $U_{\text{fs(rs)}}$ by $U_{\text{fs(rs),zn}} = \frac{U_{\text{fs(rs)}}}{N_{\text{fs(rs)}}}$ and $t_{\text{cr,fs(rs)}}$ by $t_{\text{cr,fs(rs),zn}} = \frac{h_z}{\beta_{\text{fs(rs)}}c}$. The quantities described in §4 are calculated for each slice. As the shock enters a new slice, it gradually populates that slice and the entire process of injection, acceleration and cooling is repeated. For sake of brevity, we refer to this phase of a slice as the acceleration phase in the following text. The injection and acceleration stops in the previous slice, which the shock has just left, and only the cooling continues. We refer to this phase of the slice as the cooling phase.

The photon density of a slice, along with P_{fwd} , P_{back} , and P_{side} (see §3), are used to calculate photon escape rates in all three directions, according to

$$\frac{dn_{\text{ph,fwd}}(\epsilon, \Omega)}{dt} = \frac{n_{\text{ph}}(\epsilon, \Omega)}{t_{\text{ph,esc}}} P_{\text{fwd}} \quad (38)$$

and

$$\frac{dn_{\text{ph,side}}(\epsilon, \Omega)}{dt} = \frac{n_{\text{ph}}(\epsilon, \Omega)}{t_{\text{ph,esc}}} P_{\text{side}} , \quad (39)$$

with $dn_{\text{ph,back}}(\epsilon, \Omega) = dn_{\text{ph,fwd}}(\epsilon, \Omega)$. The sideways propagating photon density becomes part of the observed spectrum originating from that slice. The forward and backward propagating photon densities are used to provide feedback to the neighbouring slices. The density of photons escaping from the region is subtracted from the total density of that slice for the current time step and the remainder is used for calculations in the next time step. We point out here that even if the volume and angle-averaged photon escape time scale for a slice turns out to be greater than the simulation time step, on average one would still expect some photons to escape out of the slice, as soon as they are created, if they happen to be produced close to the boundary. In that respect, our assumption that some percentage of photons do escape out of the region is justified and can be used to provide feedback to adjacent slices without having to track their movement individually at every time step.

The process of providing photon feedback from a particular slice to its adjacent slices, throughout the emission region (forward and reverse), at every time step accounts for the inhomogeneity in the photon density in the jet. In order to accurately calculate the SSC process, the non-local retarded-time SSC losses due to photons produced in other parts of the source need to be taken into account. These are very important for SSC dominated sources, such as TeV blazars, and thus cannot be ignored (Graff et al. 2008). Our multi-slice scheme with radiation feedback, lets us inherently address this issue without having to calculate the photon density rates at retarded times (see also Sokolov et al. 2004; Graff et al. 2008; Böttcher & Dermer 2010), along the length of the emission region. We note that our approach does not separately address the retarded-time photon field in the radial direction as calculating the SSC process in 2D is computationally more intensive and beyond the scope of this work.

5. Light Travel Time

Since photons travel with a finite speed the time delays should be incorporated in the calculation of arrival time of the radiation in the observer's frame. Different distances are covered by photons originating from different parts of the source but reaching the observer at the same time. In the case of blazars, the axis of the jet makes an angle θ_{obs}^* with the observer's line of sight. Since the emission region moves towards us, we need to take into account only the radiation that is emitted in the direction of θ_{obs}^* . Hence to calculate the time delay of the emitted photons, we consider the sideways direction for both emission regions, and the forward direction for only the forward emission region. In this section, starred quantities refer to the observer's frame, whereas primed quantities indicate the comoving frame of the emission region.

In case of the sideways direction, the time delay equation for the i^{th} slice, of width h'_z , in the emission region is given by

$$\Delta t'_{\text{side},a}(i_a) = \frac{((N_{\text{tot}} - N_b - i_a - 1)h'_{z,a} + h'_{z,b}N_b) \cos \theta'}{c}. \quad (40)$$

Here $N_{\text{tot}} = N_{\text{fs}} + N_{\text{rs}}$ is the total number of slices in the entire emission region, and θ' is the jet viewing angle given by

$$\cos \theta' = \frac{\cos \theta_{obs}^* - \beta_{sh}}{1 - \beta_{sh} \cos \theta_{obs}^*}. \quad (41)$$

The subscript 'a' stands for the fs (forward) or rs (reverse) emission region. The value of $N_b = 0$ when the time delay for the forward region is calculated and $N_b = N_{\text{fs}}$ when the same is calculated for the reverse region.

The distance calculation using Eqn 40 becomes effective only after the shocks leave a given slice. Until then, the precise location of the shock fronts is used to calculate the time delay in the sideways direction:

$$l'_{\text{fs}} = N_{\text{fs}}h'_{z,\text{fs}} - c\beta_{\text{fs}}t' \quad (42)$$

and

$$l'_{\text{rs}} = N_{\text{fs}}h'_{z,\text{fs}} + c\beta_{\text{rs}}t', \quad (43)$$

where t' is the total simulation time elapsed at the current time step. The above two equations incorporate the fact that the space in front of the shocks is still devoid of ultra-relativistic particles and hence is inactive. In the forward direction, the time delay from the forward emission region is calculated as

$$\Delta t'_{\text{up,fs}} = \frac{l'_{\text{fs}} \cos \theta'}{c} . \quad (44)$$

We carry out the forward time-delay calculation for as long as the shock is inside the forward emission region. Once the shock leaves the region, only the forward radiation originating from the slice closest to the observer’s line of sight is observed. The forward radiation from other slices provides feedback to adjacent slices.

All time delays are calculated with respect to the closest slice to the observer. In addition to the above mentioned time delays, the beaming of the radiation as observed in the observer’s frame also needs to be included. This effect is incorporated using the Doppler boosting factor, $D = [\Gamma_{\text{sh}}(1 - \beta_{\text{sh}} \cos \theta_{\text{obs}}^*)]^{-1}$, that connects the comoving frame of the emission region to the observer’s frame. The total time-delay in the reception of photons from either direction, in the observer’s frame, for the i^{th} slice of an emission region is given by

$$t_{\text{side,fs(rs);up,fs}}^{* \text{ obs}} = \frac{1 + Z}{D} (t' + \Delta t'_{\text{side,fs(rs); up,fs}}(i)) , \quad (45)$$

where Z is the redshift of the source.

The frequencies have been transformed to the observer’s frame by multiplying by D , whereas the energy fluxes per unit frequency have been transformed by multiplying by D^3 such that $(\nu F_\nu)^*$ in Jy Hz is given by

$$(\nu F_\nu)^* = \frac{D^4}{1 + Z} \frac{\dot{N}'_{\text{ph}} h \nu'^2}{4\pi d_{\text{L}}^{*2}} . \quad (46)$$

Here \dot{N}'_{ph} is the sum of the comoving photon escape rates in the forward and/or sideways direction, from both emission regions, at the current time step, and d_{L}^* is the luminosity distance to the source.

In our model, we can accomodate the case of $\cos \theta_{\text{obs}}^* < \beta_{\text{sh}}$. This would imply that in the comoving frame of the emission region, the observer is located outside the cone of superluminal motion and is looking at the region from behind. As a result, the backside of the region would be visible to the observer sooner than the front side. Thus, in this case, the observer would see the sideways and backward emission of the reverse region before seeing the sideways emission from the forward emission region. Since the emission in the direction of θ_{obs}^* needs to be considered, no radiation in the forward direction from the forward emission region would be visible to the observer.

6. Parameter Study

The combination of various input parameters dictates the overall evolution of the radiation spectrum and lightcurves in a simulation. This makes it important to understand the effects of varying such parameters in order to reproduce the observed features of a source. These parameters can be broadly categorized into shock, emission region, and jet parameters. In what follows, the unprimed quantities refer to the AGN frame, primed quantities to the comoving frame, and starred quantities indicate the observer’s frame. The shock parameters that affect the overall evolution of the SED are the kinetic luminosity, L_w , the total duration of the ejection event, t_w , the mass of the outer shell, M_o , and the widths and BLFs of the inner and outer shells, Δ_i & Γ_i and Δ_o & Γ_o . The emission region parameters that have an impact on the evolution of the radiation spectrum are the equipartition parameters, ε'_e & ε'_B (see §2.2), the particle acceleration fraction, ζ'_e , the electron acceleration rate parameter, α' , and the particle injection index, q' . Finally, the jet parameters that play a role in the evolution of the spectrum are the radius of the slices and the jet, R' , and the orientation angle of the jet, θ_{obs}^* .

We have carried out approximately 25 simulations to test and study the effects of varying the values of each of these parameters on the time-averaged simulated SEDs and their corresponding lightcurves. For all our simulations, the flux values are calculated for the frequency range $\nu' = (10^8 - 10^{26})$ Hz and electron energy distribution (EED) range $\gamma' = 10 - 10^8$ with both ranges divided into 150 grid points. The entire emission region is divided into 100 slices with 50 slices in the forward and 50 in the reverse shock region. We constrain the values of some of the parameters analytically to make sure that unphysical values are not used in the simulations. The acceleration time scale of the highest energy electron should be less than their corresponding synchrotron cooling time scale. The following condition is used to place an upper limit on the value of γ'_{max} for particles in the both forward and reverse shock emission regions:

$$\gamma'_{\text{max}} \leq \sqrt{\frac{3e}{B'\sigma_T}}, \quad (47)$$

where $e = 4.8 \times 10^{-10}$ esu is the electron’s charge in cgs units. The value of γ'_{max} should not exceed the maximum value of the EED range, mentioned above. In case of γ'_{min} , the value should not fall below the lowest value of the EED range. As pointed out by Mimica et al. (2004), the Larmor radius, r'_L , of the fastest moving (highest-energy) electron should be smaller than the slice width so that the magnetic field strength exceeds a certain minimum value and the shock acceleration can take place. This condition is used to make sure that the number of slices for both regions is selected in such a way that

$$\frac{r'_L}{h'_z} = \frac{m_e c^2}{e B'} \frac{\sqrt{\gamma'^2_{\text{max}} - 1}}{h'_z} < 1. \quad (48)$$

In order to carry out the parameter study, the value of each of the shock, emission region, and jet parameters is varied twice. We study the effects of variation in terms of changes in the flux level, spectral hardness (SH) of the simulated SED, and simulated lightcurves for different photon energies. Table 1 shows the values of the base set (run 1) parameters used to obtain the baseline model.

Table 2 shows the values of each of the parameters that are varied in the rest of the simulations. We study the effect on the simulated SED and lightcurves with respect to that of the baseline model.

Simulations 2 and 3 involve changing the value of M_o as well in order to satisfy Eqn. 1 and obtain a non-negative value of M_i , where $M_i = \frac{L_w t_w - (M_o \Gamma_o c^2)}{\Gamma_i c^2}$. On the other hand, changing the value of M_o *only* could be carried out just once because changing it in the other direction resulted in $M_i > M_o$, while we have assumed that the inner shell is the faster moving one and thus should have a relatively lower mass than the slower moving outer shell.

7. Results

Figure 4 shows the resultant time-integrated SED and lightcurves of the baseline model for a generic blazar source over an 8-day period. The input parameters chosen for the base set result in a value for the BLF of the emission region as $\Gamma_{sh} = 14.9$, with the values of BLF of the forward and reverse shocks being $\Gamma'_{fs} = 1.08$ and $\Gamma'_{rs} = 1.14$. A magnetic field value of $B' = 2.51$ G is obtained for both the forward and reverse emission regions. The values of γ'_{min} and γ'_{max} resulting from the input parameters, and evaluated using equations 21 & 18, are obtained as $\gamma'_{min,fs} = 2.18 \times 10^3$, $\gamma'_{min,rs} = 3.74 \times 10^3$, and $\gamma'_{max;fs,rs} = 8.31 \times 10^4$. The derived total width of the forward and reverse emission region is $\Delta'_{fs} = 8.19 \times 10^{15}$ cm and $\Delta'_{rs} = 9.93 \times 10^{15}$ cm, with the shock crossing time for each of the emission regions being $t'_{cr,fs} = 7.20 \times 10^5$ s and $t'_{cr,rs} = 6.94 \times 10^5$ s.

The time-integrated SED of the base set shows that the synchrotron flux peaks in the optical-near UV at $\nu_{syn}^* = 8.59 \times 10^{14}$ Hz, whereas the high-energy SSC component peaks in the MeV regime at $\nu_{SSC}^* = 8.72 \times 10^{21}$ Hz. The synchrotron to SSC transition takes place in the hard X-rays at $\nu_{turn}^* = 2.96 \times 10^{17}$ Hz, implying that synchrotron photons extend into the soft X-ray regime for this generic blazar source. The derived Compton dominance factor (CDF), defined as $CDF = \nu F_{\nu}^{SSC, peak} / \nu F_{\nu}^{syn, peak}$, is 2.90. The photon spectral index in the X-ray (2 - 10 keV) range is found to be $\alpha_{2-10keV}^* = 0.549$, whereas in the Fermi range (calculated at 10 GeV) it is $\alpha_{10GeV}^* = 2.08$.

The right side of Figure 4 shows the simulated lightcurves of the baseline model for the

Table 1. Parameter list of run 1 used to obtain the baseline model.

Parameter	Symbol	Value
Kinetic Luminosity	L_w	10^{47} erg/s
Event Duration	t_w	10^7 s
Outer Shell Mass	M_o	4×10^{31} g
Inner Shell BLF	Γ_i	25
Outer Shell BLF	Γ_o	10
Inner Shell Width	Δ_i	3×10^{15} cm
Outer Shell Width	Δ_o	6×10^{15} cm
Electron Energy Equipartition Parameter	ε'_e	5×10^{-1}
Magnetic Energy Equipartition Parameter	ε'_B	2×10^{-3}
Fraction of Accelerated Electrons	ζ'_e	2×10^{-2}
Acceleration Timescale Parameter	α'	8×10^{-6}
Particle Injection Index	q'	3.4
Slice/Jet Radius	R'_z	3×10^{16} cm
Observer Frame Observing Angle	θ_{obs}^*	3.15 deg
Redshift	z^*	0.306

Table 2. Parameter list for other simulations.

Run #	Parameter Value
2	$L_w = 5 \times 10^{47}$ ergs/s
3	$L_w = 1 \times 10^{46}$ ergs/s
4	$M_o = 1 \times 10^{32}$ g
5	$\Gamma_i = 18$
6	$\Gamma_i = 30$
7	$\Gamma_o = 5$
8	$\Gamma_o = 14$
9	$\Delta_i = 3 \times 10^{16}$ & $\Delta_o = 6 \times 10^{16}$ cm
10	$\Delta_i = 6 \times 10^{14}$ & $\Delta_o = 9 \times 10^{14}$ cm
11	$\varepsilon'_e = 9.5 \times 10^{-1}$
12	$\varepsilon'_e = 1 \times 10^{-2}$
13	$\varepsilon'_B = 1 \times 10^{-2}$
14	$\varepsilon'_B = 2 \times 10^{-5}$
15	$\zeta'_e = 9.5 \times 10^{-1}$
16	$\zeta'_e = 2 \times 10^{-3}$
17	$\alpha' = 6 \times 10^{-5}$
18	$\alpha' = 8 \times 10^{-8}$
19	$q' = 4.6$
20	$q' = 2.0$
21	$R'_z = 3 \times 10^{17}$ cm
22	$R'_z = 1.4 \times 10^{16}$ cm
23	$\theta_{\text{obs}}^* = 3.8$ deg
24	$\theta_{\text{obs}}^* = 1.15$ deg
25	$\theta_{\text{obs}}^* = 10.0$ deg

energy bands in the optical (R), X-ray (10 keV), high-energy (1 MeV), and VHE regime (1 TeV). The flux value for each energy band in all the graphs has been normalized with respect to the maximum flux value of that energy band.

The lightcurves indicate that the optical flux continues to rise as long as the shocks are present in the emission region. It peaks at $t_{\text{peak}}^* = 54$ ks. Once the shocks break out of the system, cooling dominates and the pulse begins to decline steadily. Thus, the duration for which the optical pulse lasts at its half maximum (FWHM) is 0.91 days in the observer's frame. Optical synchrotron photons are produced from higher energy electrons, which cool on a time scale shorter than the dynamical time scale of photons ($t'_{\text{dyn}} = l'_{\text{esc}}/c$) for a particular slice. Here l'_{esc} is the comoving average escape length for a photon originating anywhere in a slice. As a result, the distribution of such electrons remains steady during the acceleration phase of a slice. This implies that the total optical flux includes a contribution from the accelerating slices and the observer sees an increase in the flux due to an increase in the volume of the emission region. Once the shocks exit the respective emission regions and the cooling phase dominates the region, the optical flux decreases immediately. This makes the rising and decaying phases of the pulse almost equal leading to a quasi-symmetrical profile of the optical pulse.

On the other hand, the X-ray flux continues to rise even after the shocks exit the emission region. This happens because of two reasons: the 10 keV photons are produced from upscattering of lower energy (near IR) synchrotron photons off lower energy electrons. Such electrons remain in the system for a longer time due to slow cooling. As a result, the rise in the corresponding intensity is slow. Also, since no more electrons are added into the system during the cooling phase there is a continued increase of late-arriving photons at the sites of scattering due to the internal light crossing time effect. As a result, initially we receive the emission from the distribution that starts to cool in the back slices while the front slices are still accelerating. Once the cooling phase takes over the emission region, an important contribution comes from the front slices as the back slices have a higher number of cooled off lowest energy electrons. As a result, for a SSC dominated radiation of $\nu \sim 10^{16}$ Hz, the pulse experiences delayed peaking and decays with a long and slow tail compared to its rise. This explains why the 10 keV pulse has an asymmetrical profile and peaks last at $t_{\text{peak}}^* = 81$ ks and persists for the longest time compared to the pulses at other frequencies, with a FWHM of 1.8 days (in the observer's frame). Dividing the emission region into various slices increases the spatial resolution of the region. As a result of this enhanced resolution, when the shocks exit the system and pulses of higher synchrotron and SSC frequencies die due to the reason explained above, the 10 keV pulse, which builds up slowly over time bears the signature of this exit. The kink seen in the lightcurve of the 10 keV photons is the signature of shocks completely breaking out of the system with the forward shock - the last

shock to come out of the region - exiting the forward emission region at $t_{\text{cr}}^* = 5.27 \times 10^4$ s.

The 1 MeV photons are a result of Compton upscattering of higher energy optical photons off low energy electrons, making the pulse peak at the same time as R-band photons at $t_{\text{peak}}^* = 54$ ks. At all energies, the pulse rises sharply and declines comparatively gradually. This implies that, for the reasons explained in the case of the R-band pulse profile, the profile of the 1 MeV pulse is also quasi-symmetrical.

The very high energy (VHE) photons (1 TeV) result from the SSC scattering of higher energy (soft X-rays) synchrotron photons off higher energy electrons. As these electrons cool at a very fast rate compared to the electrons emitting at optical frequencies, the VHE photons are produced only during the acceleration phase. This is why the corresponding pulse has a sharper rise and peaks sooner than its lower energy counterparts, at $t_{\text{peak}}^* = 45$ ks. The pulse undergoes a sharp drop in the 1 TeV energy regime exactly at the time the shocks completely leave the system, thereby having the shortest pulse duration with a FWHM of 0.81 days and a nearly symmetrical profile.

For all simulations, including the baseline model, the average SED has been evaluated over an integration time of 9000 s. This facilitates comparison with observations, which usually require extended exposure times. Table 3 lists the effects of changing the values of the input parameters (according to Table 2) on the flux, the peak synchrotron and SSC frequencies (ν_{syn}^* & ν_{SSC}^* , respectively), the trough frequency (ν_{turn}^*) indicating the transition from the synchrotron to SSC component, the SH represented by energy spectral indices α^* in the 2 – 10 keV range and at 10 GeV, and the CDF of the baseline model's time-integrated SED.

Table 4 parametrizes the simulated lightcurves in terms of the time of the last shock to break out of the region, t_{cr}^* , the time at which the pulse at a given energy peaks, t_{peak}^* , and the FWHM (indicated as W^* in the table) of the pulse at a given energy.

The simulated time-integrated SEDs and the corresponding lightcurves are affected in several ways as input parameters are varied. The variation directly changes the values of some of the physical quantities like Γ'_{fs} , Γ'_{rs} , relative velocity of the shells, internal energy of the shocks, magnetic field, γ'_{min} & γ'_{max} , particle density, and size of the region, which affect the overall flux, SH, and CDF of the spectrum. This also directly alters the time at which a pulse at a given energy peaks, as well as its FWHM. We describe below some of the dominant effects observed on the simulated SED and lightcurves according to the changes in the values of the above mentioned physical quantities.

A) An increase in the internal energy of the shocks boosts the flux level of the spectrum.

Table 3. Parameter study of shock, emission-region, and jet parameters on the time-integrated SED.

Input Parameter	Value	νF_ν^*	ν_{syn}^* [Hz]	ν_{turn}^* [Hz]	ν_{SSC}^*	CDF*	SH* (2-10 keV)	SH* (10 GeV)
Baseline			8.59×10^{14}	2.96×10^{17}	8.72×10^{21}	2.90	$\alpha_{2-10\text{keV}} = 0.549$	$\alpha_{10\text{GeV}} = 2.08$
L_w	↑	↑	↑	↑	↑	3.09	↓ $\alpha_{2-10\text{keV}} = 0.682$	↑ $\alpha_{10\text{GeV}} = 2.04$
	↓	↓	↓	↑	↓	2.20	↑ $\alpha_{2-10\text{keV}} = 0.444$	↓ $\alpha_{10\text{GeV}} = 2.09$
M_o	↑	↓	↑	↑	↑	4.84	↓ $\alpha_{2-10\text{keV}} = 0.847$	↑ $\alpha_{10\text{GeV}} = 1.75$
Γ_i	↑	↑	↑	↑	↑	2.86	↓ $\alpha_{2-10\text{keV}} = 0.824$	↑ $\alpha_{10\text{GeV}} = 1.92$
	↓	↓	↓	↓	↓	2.65	↑ $\alpha_{2-10\text{keV}} = 0.441$	↓ $\alpha_{10\text{GeV}} = 2.23$
Γ_o	↑	↓	↓	↓	↓	2.34	↑ $\alpha_{2-10\text{keV}} = 0.377$	↓ $\alpha_{10\text{GeV}} = 2.36$
	↓	↑	↑	↑	↑	2.68	↓ $\alpha_{2-10\text{keV}} = 1.71$	↑ $\alpha_{10\text{GeV}} = 1.34$
$\Delta_i \& \Delta_o$	↑	↓	↓	—	↓	2.45	↑ $\alpha_{2-10\text{keV}} = 0.348$	↑ $\alpha_{10\text{GeV}} = 2.01$
	↓	↑	↑	—	↑	3.04	↓ $\alpha_{2-10\text{keV}} = 0.679$	↓ $\alpha_{10\text{GeV}} = 2.10$
ε_e	↑	↑	↑	↑	↑	4.73	↓ $\alpha_{2-10\text{keV}} = 0.993$	↑ $\alpha_{10\text{GeV}} = 1.84$
	↓	↓	↓	↓	↓	0.0386	↓ $\alpha_{2-10\text{keV}} = 1.44$	↓ $\alpha_{10\text{GeV}} = 2.39$
ε_B	↑	↑	↑	↑	↑	0.826	↓ $\alpha_{2-10\text{keV}} = 0.962$	↑ $\alpha_{10\text{GeV}} = 2.07$
	↓	↓	↓	↓	↓	33.3	↑ $\alpha_{2-10\text{keV}} = 0.087$	↑ $\alpha_{10\text{GeV}} = 1.95$
ζ_e	↑	↓	↓	↓	↓	1.86	↓ $\alpha_{2-10\text{keV}} = 0.986$	↓ $\alpha_{10\text{GeV}} = 3.45$
	↓	↑	↑	↑	↑	1.66	↓ $\alpha_{2-10\text{keV}} = 1.71$	↑ $\alpha_{10\text{GeV}} = 0.844$
α	↑	↑	—	↓	—	2.90	—	↑ $\alpha_{10\text{GeV}} = 2.07$
	↓	↓	↑	↑	↑	3.71	↑ $\alpha_{2-10\text{keV}} = 0.540$	↓ $\alpha_{10\text{GeV}} = 2.19$
q	↑	↑	—	↓	↓	3.37	↑ $\alpha_{2-10\text{keV}} = 0.340$	↓ $\alpha_{10\text{GeV}} = 2.67$
	↓	↓	↑	↑	↑	2.65	↓ $\alpha_{2-10\text{keV}} = 1.39$	↑ $\alpha_{10\text{GeV}} = 1.40$
R_z	↑	↓	↓	↓	↓	1.81	↑ $\alpha_{2-10\text{keV}} = 0.228$	↓ $\alpha_{10\text{GeV}} = 2.11$
	↓	↑	↑	↑	↑	3.07	↓ $\alpha_{2-10\text{keV}} = 0.669$	↑ $\alpha_{10\text{GeV}} = 2.04$
θ_{obs}	↑	↓	↓	↓	↓	2.92	↑ $\alpha_{2-10\text{keV}} = 0.525$	—
	↓	↑	↑	↑	↑	2.86	↓ $\alpha_{2-10\text{keV}} = 0.662$	↑ $\alpha_{10\text{GeV}} = 1.87$
outside beaming cone	↑	↓	↓	↓	↓	2.86	↑ $\alpha_{2-10\text{keV}} = 0.449$	↓ $\alpha_{10\text{GeV}} = 2.24$

Note. — The slope of the low-energy component of the time-integrated SED obtained from run 1 in the X-ray range (2-10 keV) is $\alpha_{2-10\text{keV}}^* = 0.549$ and that of the high-energy component in the Fermi range (10 GeV) is $\alpha_{10\text{GeV}}^* = 2.08$. The time-integrated low-energy component of the baseline model peaks in the optical-UV range at $\nu_{\text{syn}}^* = 8.59 \times 10^{14}$ Hz. The high-energy component peaks in the MeV range at $\nu_{\text{SSC}}^* = 8.72 \times 10^{21}$ with the transition from synchrotron to SSC component taking place in the X-rays at $\nu_{\text{turn}}^* = 2.96 \times 10^{17}$. The ↑ implies an increase in the value of a particular quantity, ↓ refers to a decrease in the value, and — stands for no change in the value. The abbreviation CDF stands for Compton Dominance Factor, defined in §7, and SH stands for Spectral Hardness, defined in §6.

Table 4. Parameter study of shock, emission-region, and jet parameters on simulated lightcurves.

Input Parameter	Value	t_{cr}^* [days]	R-Band		10 keV		1 MeV		1 TeV	
			t_{peak}^* [ks]	W^* [days]	t_{peak}^* [ks]	W^* [days]	t_{peak}^* [ks]	W^* [days]	t_{peak}^* [ks]	W^* [days]
Baseline		0.61	54	0.91	81	1.8	54	1.1	45	0.81
L_w	\uparrow	0.61	45	0.60	54	1.1	45	0.78	45	0.56
	\downarrow	0.61	45	1.1	180	3.2	99	2.3	45	0.56
M_o	\uparrow	1.6	63	1.6	162	2.1	144	2.2	54	1.5
Γ_i	\uparrow	0.55	45	0.78	72	1.8	54	1.1	45	0.95
	\downarrow	0.83	72	0.97	108	1.9	72	1.3	63	0.85
Γ_o	\uparrow	1.3	72	1.5	144	2.3	99	1.7	72	1.2
	\downarrow	0.37	18	0.34	36	1.6	18	0.68	18	1.4
$\Delta_i \& \Delta_o$	\uparrow	6.1	522	5.5	504	4.4	495	5.0	522	5.5
	\downarrow	0.11	9	0.27	18	0.97	9	0.40	0	0.26
ε'_e	\uparrow	0.61	54	0.85	72	1.8	54	1.1	45	0.76
	\downarrow	0.61	45	0.61	45	2.2	144	3.5	45	0.50
ε'_B	\uparrow	0.61	45	0.56	45	1.3	45	0.80	45	0.54
	\downarrow	0.61	63	1.39	162	2.44	99	1.7	54	1.2
ζ'_e	\uparrow	0.61	180	3.3	162	3.4	117	2.4	45	0.88
	\downarrow	0.61	45	0.64	45	0.54	45	1.7	45	0.54
α'	\uparrow	0.61	54	0.91	81	1.8	54	1.1	45	0.81
	\downarrow	0.61	45	0.62	72	1.9	45	0.94	45	0.58
q'	\uparrow	0.61	54	0.91	72	1.8	54	1.0	45	0.88
	\downarrow	0.61	45	0.88	45	1.1	54	1.3	45	0.63
R'_z	\uparrow	0.61	117	7.4	1332	28	540	18	54	0.60
	\downarrow	0.61	45	0.55	45	0.68	45	0.59	45	0.55
θ_{obs}^*	\uparrow	0.72	54	1.1	90	2.1	63	1.5	54	0.83
	\downarrow	0.40	36	0.70	54	1.3	36	0.77	27	0.81
outside beaming cone	\uparrow	2.8	234	1.9	432	5.7	252	5.1	234	2.0

Note. — The lightcurves of the baseline model are parametrized to study the effects of variation of various input parameters, listed in Table 2. We parametrize these lightcurves according to the shock crossing time, t_{cr}^* , time of peaking of a pulse at a given energy, t_{peak}^* , and full width at half maximum (FWHM), indicated as W^* , of a pulse at a particular energy.

B) An increase in the density of injected electrons increases the overall flux of the broadband spectrum. It also increases the photon number density in the region. This implies rapid radiative cooling for electrons due to synchrotron and SSC processes, and a higher value of CDF due to an increased level of SSC flux. In terms of lightcurve profiles, this translates into acceleration and cooling setting in sooner, thereby making the pulse at all energies peak sooner and last for a shorter time compared to the case where the acceleration and cooling set in more gradually.

C) An increase in the value of relative velocity of the two shells, along with the value of their individual shock propagation Lorentz factors (Γ'_{fs} & Γ'_{rs}), increases the acceleration efficiency of the collision. As a result, the overall flux of the spectrum rises. In terms of lightcurve profiles, due to efficient acceleration the particles are energized sooner and start to cool down faster. Thus, the higher the acceleration efficiency, the faster is the particle acceleration and the subsequent cooling. Hence, pulses at all energies peak sooner and last for a shorter duration of time, except for the VHE pulse. The FWHM of the VHE pulse lasts for a longer time, compared to that of the baseline model, because of efficient acceleration that energizes more particles to higher energies. As a result, high-energy electrons capable of producing TeV electrons are available for a longer time, and the FWHM of the TeV pulse increases.

D) An increase in the value of γ'_{min} implies more higher energy electrons being injected into the system. The resultant spectrum shifts toward higher frequencies. The shift in peak (ν_{syn}^* & ν_{SSC}^*) and trough (ν_{turn}^*) frequencies makes the spectrum softer in the X-ray (2 - 10 keV) but harder in the Fermi range (10 GeV). Usually the X-ray range forms the lower energy part of the SSC spectrum while the Fermi range is around or beyond the SSC peak. However, if ν_{sy}^* increases, the high-frequency end of the synchrotron component may extend into the 2 – 10 keV regime. As a result, the corresponding value of $\alpha_{2-10keV}^*$ increases, indicating a softer X-ray range spectrum. A shift of ν_{SSC}^* to higher frequencies will harden the Fermi spectrum.

E) A much lower value of γ'_{min} implies the presence of very low energy electrons in the system. This shifts the spectrum leftwards, toward lower frequencies, and higher order SSC components become prominent. This happens because the Thomson depth of the region increases and Klein-Nishina effects no longer suppress the higher-order SSC components. In terms of lightcurve profiles, this implies that acceleration and hence cooling set in very gradually for low energy electrons. On the other hand, higher energy electrons do not last for a long time in the system. As a result, photons resulting directly from these electrons are produced very early on and last for a very short time.

F) The magnetic field in the emission region is responsible for synchrotron radiation. An

increase in the value of the magnetic field decreases the synchrotron cooling time scale, which makes the synchrotron mechanism the primary mode of radiative cooling for the electrons. As a result, the synchrotron component of the spectrum becomes dominant while the photon flux due to SSC scattering decreases, thus reducing the resultant CDF value. The overall flux of the spectrum increases, but due to excessive radiative cooling the spectrum becomes softer, as it comes from a cooled population of electrons. In terms of lightcurve profiles, the shorter synchrotron cooling time scales lead to shorter pulses compared to the baseline model.

G) A larger emission region implies a larger comoving volume, but lower values of the magnetic field, shocks' internal energies, and density of injected electrons in the region. As a result, the flux and CDF of the spectrum decrease following the explanation given in (A) and (B). In terms of lightcurve profiles, since the acceleration and radiative cooling set in gradually, the pulse at a given energy peaks later and has a higher FWHM relative to that of the baseline model.

H) An increase in the value of γ'_{\max} without any change in the magnetic field value implies a shorter synchrotron cooling timescale for the highest-energy electrons. This results in more synchrotron photons in the region, thereby boosting the flux level of the SSC emission.

Subsections 7.1 - 7.3 briefly discuss the effects of varying various input parameters on the time-averaged simulated spectra and lightcurves of a generic blazar source.

7.1. Shock Parameters

Figures 5 - 7 depict the effects of varying shock parameters (L_w , M_o , Γ_i , Γ_o , and Δ_i & Δ_o) on the simulated time-integrated SED (left side) and lightcurves (right side) of the baseline model (run 1).

Increasing L_w (run 2) increases the value of the internal energy of the shocks, the magnetic field, γ'_{\min} , and the density of the injected electrons in both emission regions. Due to the reasons cited in (A), (B), and (D) the overall flux of the spectrum rises (see Fig. 5) and the SH decreases in the X-ray range but increases in the Fermi range (see Table 3). The CDF value increases marginally due to the reason cited in (B). On the other hand, decreasing L_w (run 3) from its original value results in a spectrally harder spectrum in the X-rays and a softer one in the Fermi range, along with an overall lower flux of the broadband time-integrated SED and a reduced CDF value.

Making the outer shell heavier ($\uparrow M_o$, run 4) makes the shell denser while making the

inner shell lighter and rarer. This combination of densities decreases the values of Γ_{sh} and Γ'_{fs} . The shocks' internal energies and the magnetic field values decrease along with the density of electrons injected into the forward emission region. This results in an overall decrease of the flux throughout the spectrum according to the reasons cited in (A) and (B). The $\gamma'_{\text{min,fs}}$ value decreases, whereas $\gamma'_{\text{min,rs}}$ increases due to an increase in Γ'_{rs} . Consequently, a mixed population of lower and higher energy electrons arises in the emission region during the cooling phase, giving rise to a bumpy time-integrated SED. This also leads to a comparatively longer acceleration and cooling phase in the emission region. Since the X-ray range falls in the 3rd hump of the spectrum, which forms the lower energy part of the SSC component, the spectrum is softer (see Table 3) in this case. On the other hand, an increase in $\gamma'_{\text{min,rs}}$ results in the shifting of ν_{syn}^* , ν_{turn}^* , and ν_{SSC}^* to higher frequencies. As a result, the spectrum is harder in the Fermi range, as explained in (D) and indicated by the value of $\alpha_{10\text{GeV}}^*$ in Table 3. An increase in Γ'_{rs} decreases the comoving width of the reverse emission region, thereby decreasing the comoving volume and increasing the comoving number density of electrons in the region. This leads to an increased contribution of SSC photons from the reverse emission region, thus slightly increasing the CDF value.

The lightcurves of run 2 ($L_{\text{w}} \uparrow$), 3 ($L_{\text{w}} \downarrow$), and 4 ($M_{\text{o}} \uparrow$; right side of Fig. 5) indicate a similar pattern as that of run 1. The same reasons used to explain the time of peaking of a pulse and its FWHM, at a given energy, for run 1 in §7 can be applied to runs 2, 3, and 4 to understand their pulse profiles. In case of run 2, pulses at all energies peak sooner compared to run 1, except for the TeV pulse. They also last for a shorter time due to the reasons cited in (B). The opposite holds true for run 3, although the optical pulse peaks sooner while the TeV pulse has a smaller FWHM (see Table 4) compared to run 1. This happens because the R-band synchrotron photons and the TeV Compton upscattered photons are now a result of relatively higher energy electrons, in comparison to run 1. In the case of run 4, the pulse peaks later and lasts longer at all energies compared to that of run 1 (see Table 4) due to the reasons mentioned in (B) for the case of lower particle density in the region.

A higher value of Γ_i (run 6) and a lower value of Γ_o (run 7) increase the relative velocity of the two shells along with the value of their individual shock propagation Lorentz factors ($\Gamma'_{\text{fs,rs}}$), internal shock energies, magnetic field, γ'_{min} , and density of higher energy electrons injected into the region. The overall flux of the spectrum increases (see Fig. 6) due to the reasons cited in (A), (B), and most importantly (C). In both cases, the synchrotron spectrum extends into the X-rays: for run 6 $\nu_{\text{turn}}^* \sim 6.86 \times 10^{17}$ Hz whereas for run 7 the transition from synchrotron to SSC component occurs beyond 10 keV. As a result, the spectrum is softer in the X-ray range and harder in the Fermi range (see Table 4) due to reasons given in (D). The magnetic field value for these runs is high enough to affect the CDF value according to the reason cited in (F).

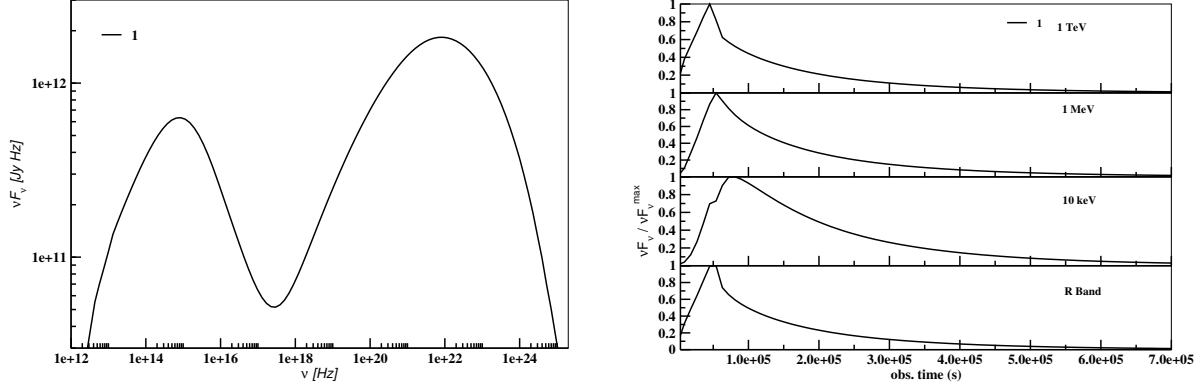


Fig. 4.— Simulated time-integrated SED (left) and lightcurves (right) of our baseline model obtained using the input parameters listed in Table 2. The panels on the right show the lightcurves that have been evaluated at various energies; from bottom to top, R band, 10 keV, 1 MeV, and 1 TeV.

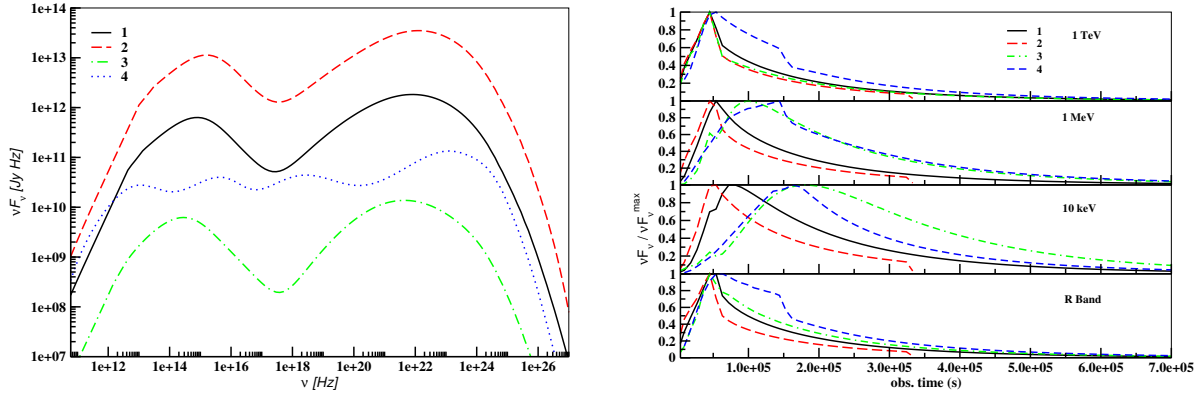


Fig. 5.— Simulated time-integrated SED and lightcurves of a generic blazar source illustrating the effects of varying shock parameters, L_w (runs 2 & 3), M_o (run 4) according to Table 2.

The lightcurves in Fig. 6 have similar profiles as that of run 1, with the same explanation as given in the lightcurve profile discussion of run 1 in §7. The pulses of runs 6 ($\Gamma_i \uparrow$) and 7 ($\Gamma_o \downarrow$) behave according to the explanation given in (C) at all energies (see Table 4).

As shown in Figure 7 and Table 3, increasing the shell widths (run 9) decreases the flux and CDF of the spectrum following the explanation given in (G). The values of the peak frequencies of both radiation components decrease relative to run 1, thus increasing the SH in the X-ray range as explained in (D) but for the case of a low value of γ'_{\min} . On the other hand, the location of the trough frequency does not change in this case. As a result, the SH for the VHE regime increases as well, as shown in Table 3.

As can be seen from Figure 7, the lightcurves from run 9 (Δ_i & $\Delta_o \uparrow$) are much more extended than those of run 1. This is because run 9 corresponds to larger widths of the colliding shells, thereby resulting in a wider emission region. As a result, the time taken for the shocks to propagate through the region is longer. Hence, pulses at all energies follow a profile as described in (G). In the case of run 9, the forward shock is the last to break out of the system, at $t_{\text{cr}}^* \sim 5.27 \times 10^5$ s, while the reverse shock exits the reverse emission region at $\sim 5.08 \times 10^5$ s.

7.2. Emission Region Parameters

As can be seen from Fig. 8, increasing the value of ϵ'_e (run 11) increases γ'_{\min} and the density of injected electrons in the region. The resultant spectrum and its SH in the X-ray and Fermi ranges, along with the value of the CDF (see Table 3), behave according to the patterns described in (B) and (D). In the case of decreasing ϵ'_e (run 12), the synchrotron component peaks in the sub-mm range ($\nu_{\text{syn}}^* \sim 6.21 \times 10^{11}$ Hz) with the transition from the synchrotron to the SSC component taking place in the optical ($\nu_{\text{turn}}^* \sim 6.50 \times 10^{14}$ Hz). The MeV photons are a result of higher order SSC scattering. The spectrum becomes softer in both X-ray and Fermi range (see Table 3) because the entire spectrum shifts toward low frequencies, due to an extremely low value of γ'_{\min} .

Increasing ϵ'_B (run 13) increases the magnetic field while marginally increasing γ'_{\min} and the normalization of the injected electron spectrum. The spectral flux, its SH, and the corresponding CDF value undergo the same changes as cited in (F), and (D).

As can be seen from Fig. 8 and Table 3, the lightcurve profiles of run 11 ($\epsilon'_e \uparrow$) follow a similar pattern to those of run 1 at all energies. In the case of run 12 ($\epsilon'_e \downarrow$), since R-band photons lie in the highest energy part of the synchrotron component (see Fig. 8), the high energy electrons responsible for these photons last for a short time in the system. As a

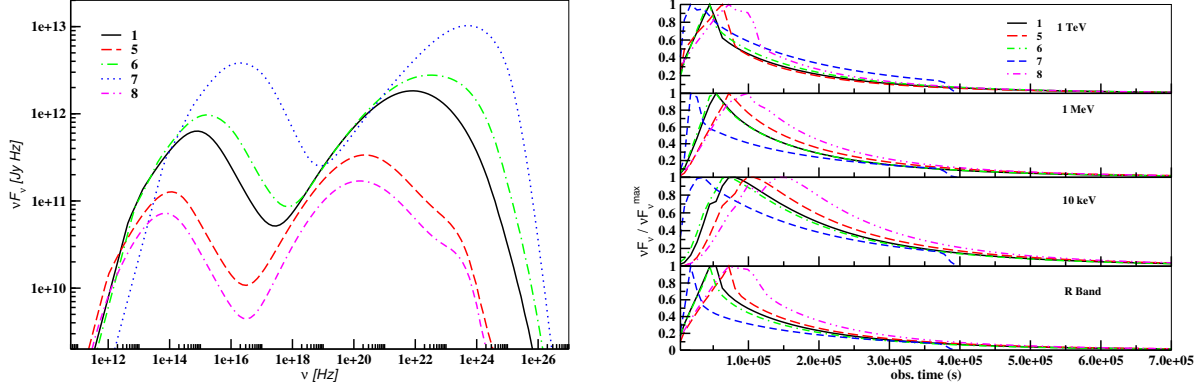


Fig. 6.— Simulated time-integrated SED and lightcurves of a generic blazar source illustrating the effects of varying shock parameters Γ_i (runs 5 & 6) and Γ_o (runs 7 & 8) according to Table 2.

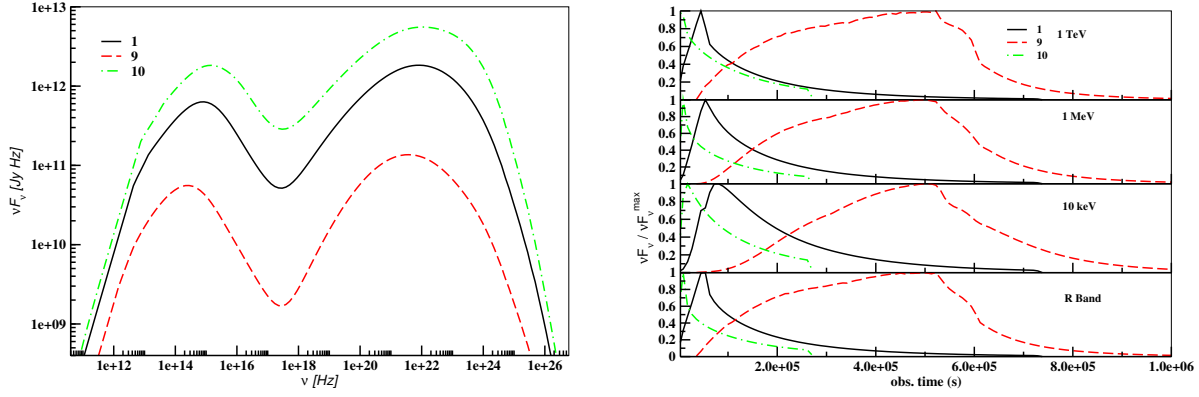


Fig. 7.— Simulated time-integrated SED and lightcurves of a generic blazar source illustrating the effects of varying shock parameters Δ_i & Δ_o (runs 9 & 10) according to Table 2.

result, the corresponding pulse peaks sooner with a smaller FWHM relative to run 1. On the other hand, the X-ray photons form the higher energy part of the 1st order SSC component and are the result of scattering of high energy synchrotron photons off low energy electrons. Thus, the corresponding pulse peaks sooner relative to run 1 but has maximum contribution from cooling, and therefore a larger FWHM. The MeV photons form the lower energy part of the higher order SSC component and result from the higher order SSC scattering of SSC photons off lower energy electrons. Thus, the pulse at MeV energies peaks later and lasts for a longer time than that of run 1. The TeV photons are a result of higher order SSC scattering off high energy electrons. Since such electrons last for a very short time in the system, the pulse has a fairly equal contribution from both acceleration and cooling, making it approximately symmetric about its maximum (see Fig. 8). As can be seen from Fig. 8 and Table 4, the pulses in run 13 ($\varepsilon'_B \uparrow$) follow the same pattern as explained in (F).

As shown in Figure 9 and Table 3, increasing ζ'_e (run 15) increases the fraction of accelerated electrons in the region while decreasing the value of γ'_{\min} and the density of injected high-energy electrons. The effects on the spectrum can be explained using reasons given in (E), and (B) for the case of lower density of electrons. As can be seen from the figure, the synchrotron component for this case peaks in the IR instead of the optical, as in run 1. Thus, the optical photons form the lower energy part of the SSC component and are produced from the SSC scattering of much lower energy synchrotron (radio) photons off the lowest energy electrons. Hence, the higher order SSC component peaks at ~ 1 MeV and is a result of upscattering of first-order SSC photons off low energy electrons. On the other hand, the TeV photons are the result of higher order SSC scattering of SSC photons off the highest-energy electrons. The spectrum in the X-ray range becomes softer (see Table 3) because, as can be seen from the figure, the transition between the SSC and the higher order SSC components lies in the 2-10 keV energy range. On the other hand, the spectrum in the Fermi range becomes softer due to the shift in ν_{SSC}^* to lower frequency.

As can be seen from Fig. 9 and Table 3, increasing the value of α' (runs 17) increases the value of γ'_{\max} while mildly decreasing the value of γ'_{\min} and the normalization of the injected electron spectrum. As a result, the SH of the spectrum and the CDF value are hardly affected (see Table 3), but the overall flux of the spectrum increases due to the reasons given in (H).

As can be seen from the right side of Figure 9, pulse profiles of all runs at all energies follow the same trend as described in §7 for run 1. In the case of run 15 ($\zeta'_e \uparrow$), since the particle density of the region decreases the t_{peak}^* and FWHM of a pulse at a given energy follow the same explanation as given in (B) for that case. As can be seen from Fig. 9 and Table 4, the pulse profiles of run 17 ($\alpha' \uparrow$) are highly similar at all energies to that of run 1,

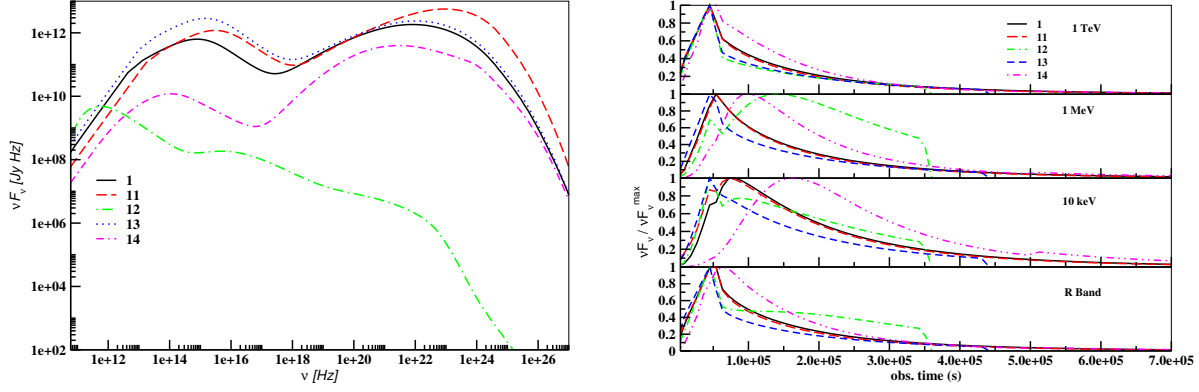


Fig. 8.— Simulated time-integrated SED and lightcurves of a generic blazar source illustrating the effects of varying emission region parameters ε'_e (runs 11 & 12), and ε'_B (runs 13 & 14) according to Table 2.

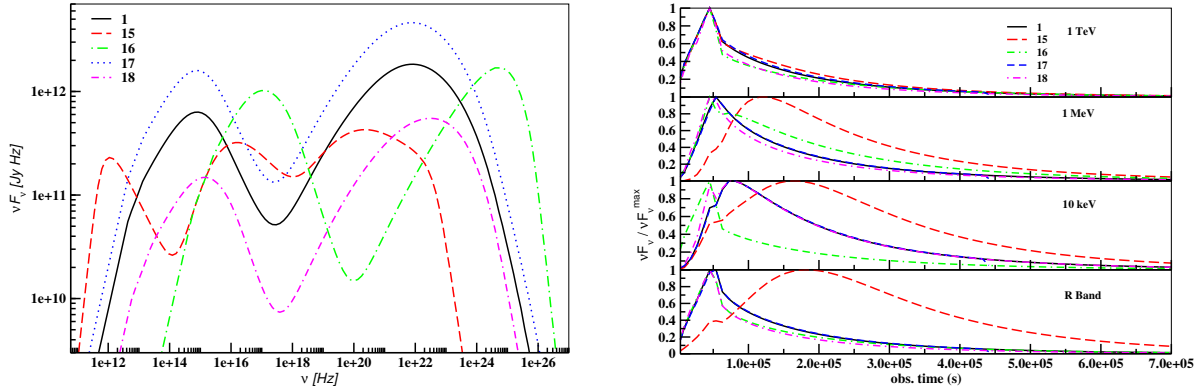


Fig. 9.— Simulated time-integrated SED and lightcurves of a generic blazar source illustrating the effects of varying emission region parameters, ζ'_e (runs 15 & 16), and α' (runs 17 & 18) according to Table 2.

as are their t_{peak}^* and FWHM values.

Increasing the value of q' (run 19) increases γ'_{min} slightly along with the normalization of the injected electron spectrum, while keeping the magnetic field value the same. Thus, the overall flux level of the SED rises along with the value of the CDF, as explained in (B). Since a softer population of electrons is injected into the region, the peak and trough frequencies shift toward lower frequencies, even though the value of γ'_{min} increases slightly. As a result, the SH in the X-ray and Fermi ranges are affected according to (D), but for the case of a lower value of γ'_{min} .

The lightcurves from run 20 ($q' \downarrow$) (Figure 10) show that a harder energy distribution of the electron population results in a sharper rise and a steeper decline of the pulse. Since the parent population of electrons is more energetic than that of runs 1 (base set) & 19 ($q' \uparrow$), the electrons lose their energy faster and more energetic synchrotron photons (hard X-rays; Figure 10) are produced, although only for a short time. As a result, the rise in the corresponding pulses at X-ray and optical energies is sooner and the FWHM shorter compared to those of runs 1 & 19. For the blazar source under consideration, since TeV photons are a result of SSC scattering of higher energy (soft X-rays) photons off higher energy electrons, they are produced simultaneously with the lower energy (optical) synchrotron photons but with the shortest FWHM (see Table 4). The TeV photons would lag behind the soft X-ray synchrotron photons by a time of the order of the cooling time scale for these synchrotron photons. The MeV pulse peaks the last and lasts the longest relative to that of run 1 & 19 because for this case, they are a result of SSC scattering of lower energy (optical) synchrotron photons off low energy electrons.

7.3. Jet Parameters

As can be seen from Fig. 11, increasing R'_z (run 21) implies a larger emission region. This decreases the overall flux of the SED and the CDF value (see Table 3) following the reasons given in (G). Since the value of γ'_{min} decreases slightly in this case, the peak and trough frequencies, along with the SH, in both energy ranges are affected in the opposite way to what is explained in (D).

For run 21 ($R'_z \uparrow$), the pulse profiles at all energies (except at TeV) are much more extended relative to run 1 (see Table 4) due to the reasons explained in (G). Since the width of the emission region for both runs 21 & 22 ($R'_z \downarrow$) remains the same, the shock crossing time does not change. As a result, the TeV pulse lasts only for as long as the shocks are present in the system. Thus, the FWHM of the pulse is almost the same as the shock crossing time

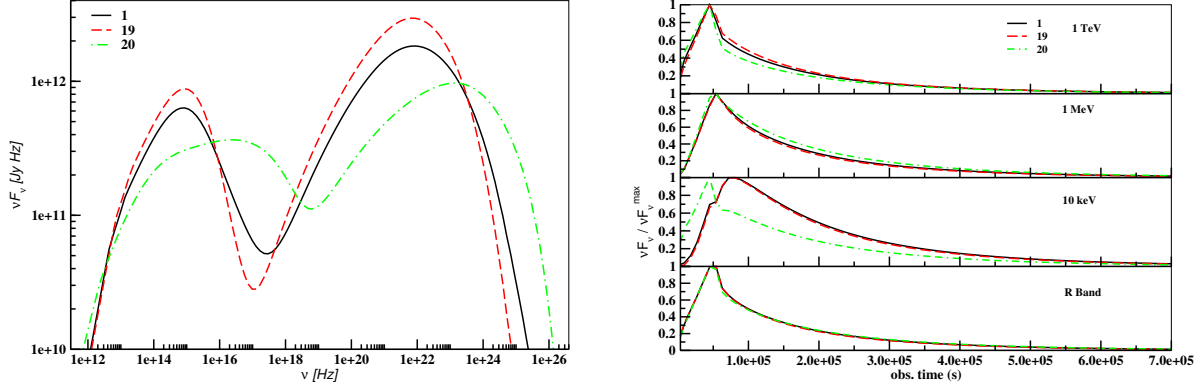


Fig. 10.— Simulated time-integrated SED and lightcurves of a generic blazar source illustrating the effects of varying emission region parameter q' (runs 19 & 20) according to Table 2.

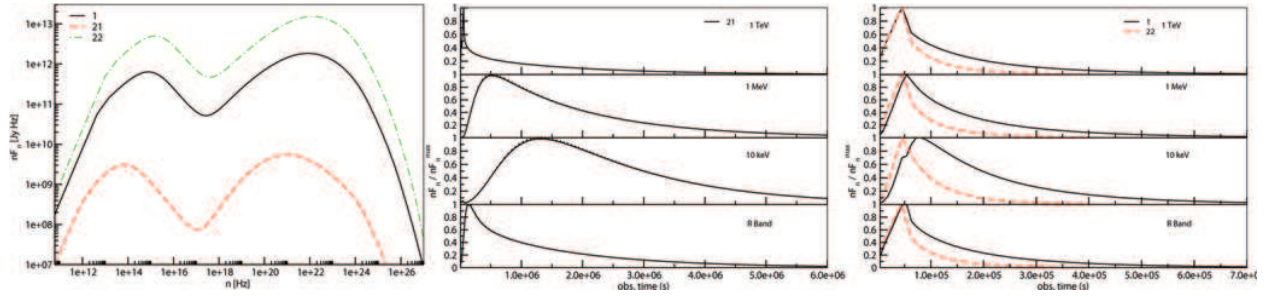


Fig. 11.— Simulated time-integrated SED and lightcurves of a generic blazar source illustrating the effects of varying jet parameter R'_z (runs 21 & 22) according to Table 2.

($t_{\text{cr}}^* \sim 0.61$ days, in the observer’s frame) of the forward shock.

As can be seen from Figure 12 and Table 3, decreasing the value of θ_{obs}^* (run 24) increases the overall flux of the spectrum without changing the values of magnetic field, the shocks’ internal energies, γ'_{min} , γ'_{max} , and the particle density. Since the jet is now closely aligned with our line of sight, the overall radiation is boosted more strongly in our direction, thereby increasing the overall flux. Due to a lower value of θ_{obs}^* , the frequencies when transformed into the observer’s frame assume higher values. As a result, even though the synchrotron and SSC components peak at the same location in the comoving frame, in the observer’s frame the values of ν_{syn}^* , ν_{turn}^* , and ν_{SSC}^* shift to higher frequencies. This does not affect the CDF value, as can be seen from Table 3 for all three runs 23, 24, and 25. However, in the case of run 24, this shift of the spectrum towards higher frequencies causes the synchrotron component in the observer’s frame to extend more into the X-rays, with the transition from synchrotron to SSC component taking place at $\nu_{\text{turn}}^* \sim 4.53 \times 10^{17}$ Hz. As a result, the spectrum in the 2-10 keV range appears to be softer as the synchrotron component begins to contribute to the soft X-ray flux. On the other hand, the SSC component in the observer’s frame peaks at $\nu_{\text{SSC}}^* \sim 1.34 \times 10^{22}$ Hz, with the entire hump extending further into the Fermi range. This makes the spectrum in the 10 GeV range appear harder, as can be seen from the value of $\alpha_{10\text{GeV}}^*$ in Table 3.

We consider two cases of a larger value of θ_{obs}^* . The first one is run 23, where the value of θ_{obs}^* increases such that $\cos \theta_{\text{obs}23}^* > \beta_{\text{sh}}$ and the line of sight is still within the cone of maximum superluminal motion. The second one is run 25 where the value of θ_{obs}^* is high enough to put the line of sight outside the beaming cone. In the comoving frame, this would translate into the observer looking at the emission region from behind, as a result of which the backside of the region would become visible to the observer before the front side does. As shown in Fig. 12 and Table 3, for both runs 23 & 25 the opposite trend, compared to run 24, is observed. Since the value of θ_{obs} in run 25 is higher than that of run 23, the effect on the overall flux, the frequency shift, and the SH of the spectrum is even more dramatic compared to that of run 23.

The lightcurves of runs 23 ($\theta_{\text{obs}}^* \uparrow$), 24 ($\theta_{\text{obs}}^* \downarrow$), and 25 ($\theta_{\text{obs}}^* \uparrow$, outside beaming cone) are all shifted in time with respect to those of run 1 (see Fig. 12). In the case of run 24, since the value of θ_{obs}^* is smaller, the required time for photons at all energies to reach from the far side to the near side, of the jet emission region, is reduced. As a result, the pulses at all energies peak sooner and last for a shorter duration of time compared to those for run 1 (see Table 4). Due to a smaller θ_{obs}^* , the shock crossing time of the forward shock for run 24, in the observer’s frame, turns out to be shorter than that for run 1. As a result, the kink that is present in the lightcurve of 10 keV photons for run 1, indicating the time of exit of

the shock from the system, is smeared out to give a smoother pulse profile at that energy. The exact opposite effect can be seen in the pulse profiles at all energies of run 23. In the case of run 25, since the line of sight, in the comoving frame of the emission region, passes through the region from behind, the light travel time increases by a significant amount. This stretches the entire pulse profiles at all energies compared to runs 1, 23, & 24. Once again, the value of t_{peak}^* for R-band and TeV photons almost marks the time when the shock breaks out of the system for all the three runs.

8. Summary And Conclusions

We have developed a 1D multi-slice internal shock model with radiation feedback scheme to simulate the radiative signatures of blazars in a time-dependent manner. We consider a cylindrical geometry for the emission region and semi-analytically compute the volume and angle-averaged photon escape time scale for it. The inclusion of radiation feedback through a multi-slice scheme makes our model a powerful tool to address the issue of inhomogeneity in the photon and particle density throughout the emission region. Under this scheme, the cylindrical emission region is divided into multiple slices and the subsequent time-dependent radiation transfer, within each slice and in between slices, is calculated by using the appropriate photon escape rates of the slices. Our scheme inherently addresses the non-locality and time-delay effects due to internal light-travel time while calculating the SSC emission of a blazar source. By increasing the spatial resolution along the length of the emitting region and considering the contribution of all slices in the emission region, our model mimicks an inhomogeneous source where the observer sees photons from a mixed population of electrons of various ages. Such a scenario is important for cases where the electron population evolves on time scales shorter than the dynamical time. Thus our approach facilitates the simulation of high-energy variability observed in blazars, especially the SSC dominated TeV sources, more accurately. Our model includes synchrotron and SSC emission for evaluating the self-consistent time-dependent radiation transfer along the length of the emission region. We account for the light travel time delays, in our model, to evaluate the radiative output in the observer's frame.

We consider a single inelastic collision between two shells of plasma of different mass, velocity, and energy. The collision results in the formation of a forward and a reverse shock, internal to the jet. The relativistic shocks are separated by a contact discontinuity (CD). We use the relativistic hydrodynamic Rankine-Hugoniot jump conditions to obtain the characteristics of the shock dynamics. The bulk Lorentz factor (BLF) of the emission region in the lab frame is evaluated using the equality of pressures of the shocked fluids

across the CD.

The emission region parameters, such as γ_{\max} , γ_{\min} , the normalization of the injected electron spectrum, and the magnetic field, B , are obtained using the BLFs of the shocks and the width of the emission region in the comoving frame of the shocked fluid. The emission region parameters are then used to evaluate the radiation spectrum resulting from the collision for a cylindrical emission region. A numerical simplification of the synchrotron emission formula has been used in order to speed up the computing time. Synchrotron spectra calculated with this numerical simplification match those calculated with the exact expression to a relative accuracy of better than 1 %.

The code has been tested to satisfy various analytical constraining conditions. We have carried out 25 simulations to perform an extensive parameter study of the code, in order to understand the effects of varying various shock (wind luminosity, mass of the outer shell, BLF and width of the two shells), emission-region (fraction of shock energy stored in the electron and magnetic field energy density, fraction of effectively accelerated electrons, acceleration timescale parameter, and particle energy index), and jet parameters (radius of the slice/jet, and observing angle inside and outside of the beaming cone) on the resulting SED and spectral lightcurves of a generic blazar source. The SED has been parametrized on the basis of the change in the level of its overall flux, shift in its peak and trough frequencies, change in its spectral hardness in the 2 - 10 keV and 10 GeV energy ranges, and the Compton dominance of the SSC component over the synchrotron component. The lightcurves at optical, X-ray, MeV, and TeV energy ranges have been parametrized on the basis of the time of exit of the shock from the emission region, the time of the peak, and the FWHM of a pulse at a given energy.

As demonstrated in §6, both SEDs and lightcurves give us an idea about the dominant radiation mechanism responsible for producing radiation of a particular frequency and the corresponding time lags between various frequency bands. As shown in §6, our model can be exploited to reproduce long and short-term variability of blazars based on the combination of shock, emission-region, and jet parameters. The symmetric and asymmetric profiles observed in the lightcurves of blazars are frequency dependent. Lightcurves at higher synchrotron and SSC frequencies tend to be more symmetric than their lower frequency counterparts (see e.g., Chiaberge & Ghisellini 1999; Sokolov et al. 2004) for the reasons explained in §6. As indicated in §6, such profiles of the lightcurves can be reproduced using the right combination of shock, emission-region, and jet parameters. The symmetric and asymmetric profiles of the lightcurves are also dependent on the angle at which the jet is being viewed (see Fig. 12). As mentioned below, since we are not carrying out a 2-D simulation of the jet radiation processes, we are limited by the internal light crossing time in the radial direction. As a result, the

symmetric profiles that appear from viewing the jet at non-zero angles (Sokolov et al. 2004) and are dominated by light crossing time effect across the emission region are not accounted for.

The particle injection spectra can be used to identify the characteristic signatures of various particle acceleration mechanisms. The particle acceleration at parallel shocks can give rise to electron spectra following a power-law distribution with an injection index of $q' \sim 2.2 - 2.3$ (Achterberg et al. 2001; Gallant et al. 1999). Oblique shocks, on the other hand, are believed to produce much softer injection spectral indices with $q' > 2.3$ (Ostrowski & Bednarz 2002; Niemiec & Ostrowski 2004). In contrast, 2nd order Fermi acceleration might result in a harder injection index of the order of $q' \sim 1$ or beyond if the plasma is turbulent, behind the shock front. Thus, the value of q' used for modeling the SED and spectral lightcurves of a blazar source can give us insights on the kind of shock propagating through its jet and the dominant mode of acceleration present in the source. Our future modeling efforts will help us gain a deeper understanding of the real data.

We would like to point out that for simplicity we have considered the role of the magnetic field to be negligible in the dynamics of the shock energetics. The structure of the mean large scale magnetic field plays an important part in particle acceleration and shock dynamics. We also emphasize that for making the problem at hand more tractable we chose to have the particle injection spectral index, q , as a free parameter. The value of q should really be the result of shock dynamics and the underlying magnetic field structure. In our model, the escape timescale for electrons from the emitting region is a weakly constrained, free parameter. It involves a fudge factor that parametrizes the randomness of the magnetic field direction. Hence a more detailed model of the radiation transfer in blazar jets, dealing with particle acceleration, must address these physical parameters.

We note that our model, in its current form, does not address the internal light travel time in the radial direction. The time resolution of our model is limited by the light crossing time across the cylinder. This feature is more relevant for carrying out a comparison between synchrotron and SSC peak times at highest frequencies, especially for the case where the jet is being viewed face-on (Sokolov et al. 2004). A 2-D multi-celled approach would be a more appropriate tool to incorporate this aspect of frequency-dependent time lags.

We thank Prof. Alan Marscher for comments and discussions. We acknowledge Dr. Justin Finke for useful suggestions. We thank the anonymous referee for his/her helpful comments. The work of M.B. is supported by NASA through Fermi Guest Investigator Grant NNX09AT82G and Astrophysics Theory Program Grant NNX10AC79G. The work of M.J. is partially supported through NRL BAA 76-03-01, contract no. N00173-05-P-2004 (Ohio

University) and National Science Foundation grant AST-0907893 from Boston University.

A. Coefficients of Γ_{sh}

The coefficients of Eqn. 11 are as follows:

$$\begin{aligned} a &= \hat{\gamma}^2 [(Y - 1)^2 + 4Y (n - 2x^2m)] , \\ b &= 2\hat{\gamma}g [(Y + 1) (\Gamma_o + Y\Gamma_i) - 2Yxpm] , \\ c &= 2\hat{\gamma}Y (2 - 3\hat{\gamma}) n + 2\hat{\gamma} (\hat{\gamma} - 2) r - 2Yxm (g^2 - 4\hat{\gamma}^2x) - 4Y\hat{\gamma}g + (1 - \hat{\gamma}^2) (1 + Y^2) , \\ d &= 2g [Yp (1 + \hat{\gamma} (x (1 - 2q) - 1)) - (1 + \hat{\gamma}) (\Gamma_o + Y^2\Gamma_{rmi}) + \hat{\gamma} (\Gamma_o^3 + Y^2\Gamma_i^3)] , \\ e &= \hat{\gamma}^2 (\Gamma_o^4 + Y^2\Gamma_i^4) + 2\hat{\gamma}Y (2 - gn - \hat{\gamma} (1 + x^2)) + r (1 - \hat{\gamma}^2) - 2g^2Yxq - 2Y . \quad (\text{A1}) \end{aligned}$$

Here, $x = \Gamma_o\Gamma_i$, $m = 1 - \beta_o\beta_i$, $q = \beta_o\beta_i$, $n = \Gamma_o^2 + \Gamma_i^2$, $p = \Gamma_o + \Gamma_i$, $r = \Gamma_o^2 + Y^2\Gamma_i^2$, $g = 1 - \hat{\gamma}$, and $Y = \bar{\rho}_i/\bar{\rho}_o$. All unprimed quantities refer to the AGN frame and quantities with an overline refer to the unshocked fluid frame.

B. Photon Escape Time Calculation

All quantities mentioned here refer to the comoving frame of the emission region. The intermediate steps used to derive equation (27) are the following:

As shown in Figure 13 (a), $l_{\text{crit}+}$ is the distance traveled by a photon that escaped from the edge of the region in the forward direction, at an angle $\theta_{\text{crit}+}$ with the z-axis, and similarly for $l_{\text{crit}-}$ at an angle $\pi - \theta_{\text{crit}-}$ with the z-axis; b is the corresponding projection of these lengths on the horizontal plane (Figure 13 (b)).

Using the law of cosines and solving the quadratic equation in b , and realizing that negative distances are unphysical, an expression for b can be obtained as

$$b = \sqrt{R^2 - r^2 \sin^2 \phi} - r \cos \phi . \quad (\text{B1})$$

Now, referring to Figure 13, we can write

$$\tan \theta_{\text{crit}+} = \frac{b}{h - z}, \tan \theta_{\text{crit}-} = \frac{-b}{z},$$

$$\begin{aligned}
l_{\text{esc}-} &= \frac{-z}{\mu_-} & \text{for } -1 < \mu < \mu_{\text{crit}-}, \\
l_{\text{esc}} &= \frac{b}{\sqrt{1-\mu^2}} & \text{for } \mu_{\text{crit}-} < \mu < \mu_{\text{crit}+}, \\
l_{\text{esc}+} &= \frac{h-z}{\mu_+} & \text{for } \mu_{\text{crit}+} < \mu < +1, \\
\mu_{\text{crit}+} &= \frac{h-z}{\sqrt{b^2+(h-z)^2}}, \mu_{\text{crit}-} = \frac{-z}{\sqrt{b^2+z^2}}.
\end{aligned} \tag{B2}$$

Substituting equations (B2) in equation (26) and then equation (26) in (25), equation (25) can be written as

$$\begin{aligned}
\langle t_{\text{ph,esc,V}} \rangle &= \left(\frac{1}{\pi R^2 h} \right) \left(\frac{1}{4\pi c} \right) \int_0^{2\pi} \int_0^R \int_0^h \\
&\left(\int_0^{2\pi} d\Phi \left[\int_{-1}^{\mu_{\text{crit}-}} l_{\text{esc}-} d\mu_- + \int_{\mu_{\text{crit}-}}^{\mu_{\text{crit}+}} l_{\text{esc}} d\mu + \int_{\mu_{\text{crit}+}}^{+1} l_{\text{esc}+} d\mu_+ \right] \right) d\phi r dr dz,
\end{aligned} \tag{B3}$$

which gives

$$\begin{aligned}
\langle t_{\text{ph,esc,V}} \rangle &= \left(\frac{1}{\pi R^2 h} \right) \left(\frac{1}{4\pi c} \right) \int_0^{2\pi} \int_0^R \int_0^h \\
&\left(\int_0^{2\pi} d\Phi \left[\int_{-1}^{\mu_{\text{crit}-}} \frac{-z}{\mu_-} d\mu_- + \int_{\mu_{\text{crit}-}}^{\mu_{\text{crit}+}} \frac{b}{\sqrt{1-\mu^2}} d\mu + \int_{\mu_{\text{crit}+}}^{+1} \frac{h-z}{\mu_+} d\mu_+ \right] \right) d\phi r dr dz.
\end{aligned} \tag{B4}$$

Carrying out integration over μ , and realizing that the integration of the right hand side expression over the angle Φ is going to give 2π , the above equation can be written as

$$\langle t_{\text{ph,esc,V}} \rangle = \frac{2}{R^2 h} \int_0^R \left(\int_0^h \left(\frac{1}{2c} [(z-h) \ln(h-z) - z \ln z] + I_1 + I_2 + I_3 \right) dz \right) r dr, \tag{B5}$$

where

$$\begin{aligned}
I_1 &= \frac{h-z}{8\pi c} \int_0^{2\pi} \ln(b^2 + (h-z)^2) d\phi, \\
I_2 &= \frac{z}{8\pi c} \int_0^{2\pi} \ln(b^2 + z^2) d\phi, \\
I_3 &= \frac{1}{4\pi c} \int_0^{2\pi} b \left[\arcsin\left(\frac{h-z}{\sqrt{b^2 + (h-z)^2}}\right) + \arcsin\left(\frac{z}{\sqrt{b^2 + z^2}}\right) \right] d\phi. \tag{B6}
\end{aligned}$$

The above three integrals can be solved semi-analytically to obtain the final expression for the volume and angle-averaged photon escape timescale for a cylindrical region given in Eqn. (27).

C. Synchrotron Function Fitting

All quantities mentioned here refer to the comoving frame of the emission region. The function $R(x)$, used in the calculation of the synchrotron photon production density rate (see §4, Eqn. 31), is given by (Crusius & Schlickeiser 1986)

$$R(x) = \frac{\pi x}{2} [W_{0, \frac{4}{3}}(x) W_{0, \frac{1}{3}}(x) - W_{\frac{1}{2}, \frac{5}{6}}(x) W_{\frac{-1}{2}, \frac{5}{6}}(x)] , \tag{C1}$$

where $x = \frac{4\pi m_e c \nu}{3eB\gamma^2}$ is the normalized frequency, and $W_{\lambda, \mu}(x)$ denotes Whittaker's function (Abramowitz & Stegun 1970).

In order to save CPU time while computing equation (31) (§4), we numerically approximate the function, $R(x)$, as follows:

$$R(x) = C_1 x^{p_1} e^{-x} - C_2 x^{-p_2} e^{-x} , \tag{C2}$$

where $C_1 = 1.08895$, $C_2 = 2.35861 \times 10^{-3}$, $p_1 = 0.20949$, and $p_2 = 0.79051$.

The asymptotic expansions of Whittaker functions (Crusius & Schlickeiser 1986) that are used in the calculation of Eqn. 31, for small ($x \ll 1$) and large ($x \gg 1$) values of x , are no longer required when using the above approximation. Since $R(x)$ has been approximated for the expression given in Eqn. (C1), we normalize $R(x)$ at lower values of x , where $R(x)$

$\propto x^{1/3}$. This is carried out to obtain a good fit to the exact expression for the entire range of x values.

Figure 14 shows the comparison of simulated SEDs of a generic blazar source, obtained from using the approximation and the exact expression. As shown in the figure, the approximation is accurate to better than 1% over the entire frequency range.

REFERENCES

- Achterberg, A., Gallant, Y. A., Kirk, J. G., & Guthmann, A. W., 2001, MNRAS, 328, 393
- Abramowitz, M., & Stegun, I. A., 1970, Handbook of mathematical functions: with formulas, graphs, and mathematical tables, National Bureau of Standards
- Aharonian et al., 2007, ApJL, 664, 71
- Albert et al., 2007, ApJ, 669, 862
- Blandford, R. D., & McKee, C. F., 1976, Phys. Fluids, 19, 1130
- Bloom, S. D., & Marscher, A. P., 1996, ApJ, 461, 657
- Böttcher, M., & Bloom, S. D., 2000, AJ, 119, 469
- Böttcher, M., & Chiang, J., 2002, ApJ, 581, 127
- Böttcher, M., & Dermer, C. D., 2010, ApJ, 711, 445
- Böttcher, M., Mause, H., & Schlickeiser, R., 1997, A&A, 324, 395
- Böttcher, M., & Schlickeiser, R., 1997, A&A, 325, 866
- Catanese, M., & Weekes, T. C., 1999, PASP, 111, 1193
- Chiaberge, M., & Ghisellini, G., 1999, MNRAS, 306, 551
- Chiang, J., & Dermer, C. D., 1999, ApJ, 512, 699
- Costamante, L., & Ghisellini, G., 2002, A&A, 384, 56
- Crusius, A., & Schlickeiser, R., 1986, A&A, 164, 16
- deJager, O. C., & Harding, A. K., 1992, ApJ, 396, 161

- Dermer, C. D., & Schlickeiser, R., 1993, *ApJ*, 416, 458
- Gaidos, J. A., et al., 1996, *Nature*, 383, 319
- Gallant, Y. A., et al., 1999, *A&AS*, 138, 549
- Georganopoulos, M., & Marscher, A. P., 1998, *ApJ*, 506, 621
- Gradshteyn, I. S., & Ryzhik, I. M., 1994, *Table of integrals, series and products*, New York: Academic Press
- Graff, P. B., et al., 2008, *ApJ*, 689, 68
- Jones, F. C., 1968, *Phys. Rev.*, 167, 1159
- Jorstad, S. G., et al., 2005, *AJ*, 130, 1418
- Joshi, M., & Böttcher, M., 2007, *ApJ*, 662, 884
- Kirk, J. G., Rieger, F. M., & Mastichiadis, A., 1998, *A&A*, 333, 452
- Kobayashi, M., Piran, T., & Sari, R., 1997, *ApJ*, 490, 92
- Longair, M. S., 1994, *High energy astrophysics. Vol.2: Stars, the galaxy and the interstellar medium*, Cambridge: Cambridge University Press
- Marscher, A. P., & Gear, W. K., 1985, *ApJ*, 298, 114
- Maraschi, L., Ghisellini, G., & Celotti, A., 1992, *ApJ*, 397, L5
- Mimica, P., et al., 2004, *A&A*, 418, 947
- Niemiec, J., & Ostrowski, M., 2004, *ApJ*, 610, 851
- Ostrowski, M., & Bednarz, J., 2002, *A&A*, 394, 1141
- Panaitescu, A., & Mészáros, P., 1999, *ApJ*, 526, 707
- Press W. H., et al., 1992, *Numerical Recipes in C*, Cambridge: Cambridge University Press
- Rieger, F. M., & Duffy, P., 2004, *ApJ*, 617, 155
- Rybicki, G. B., & Lightman, A. P., 1979, *Radiative processes in astrophysics*, John Wiley & Sons, New York
- Sambruna, R. M., et al., 2007, *ApJ*, 670, 74

Sikora, M., Begelman, M. C., & Rees, M. J., 1994, *ApJ*, 421, 153

Sikora, M., et al., 2001, *ApJ*, 554, 1

Sokolov, A., Marscher, A. P., & McHardy, I. M., 2004, *ApJ*, 613, 725

Spada, M., et al., 2001, *MNRAS*, 325, 1559

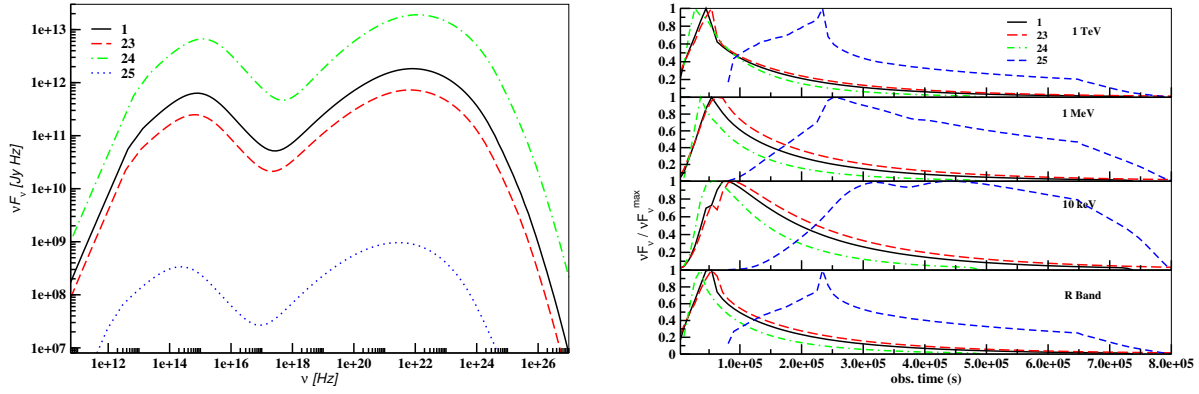


Fig. 12.— Simulated time-integrated SED and lightcurves of a generic blazar source illustrating the effects of varying jet parameter θ_{obs}^* (runs 23, 24 & 25) according to Table 2.

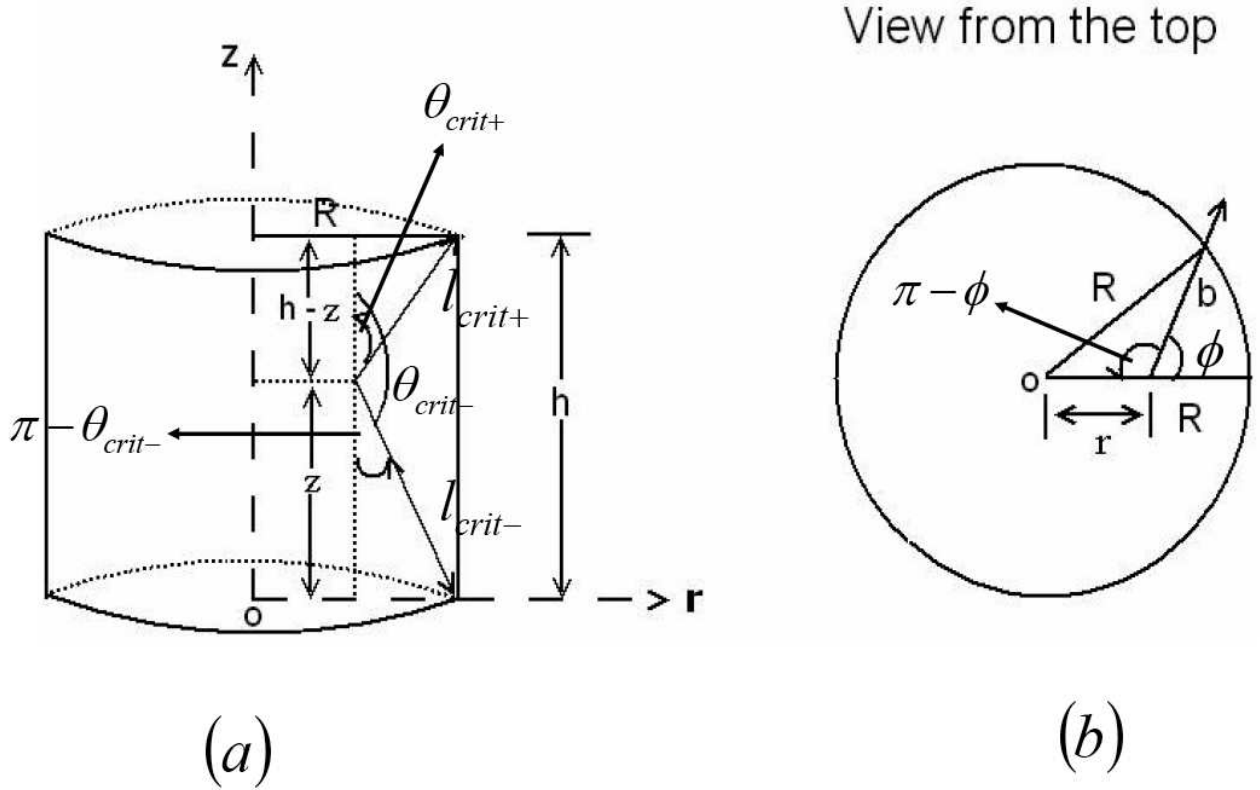


Fig. 13.— In (a) we illustrate the three angles of escape along with their corresponding escape lengths. In (b) we show the angle consideration and the projection of the escape lengths on the horizontal plane of the cylinder, when viewed from the top.

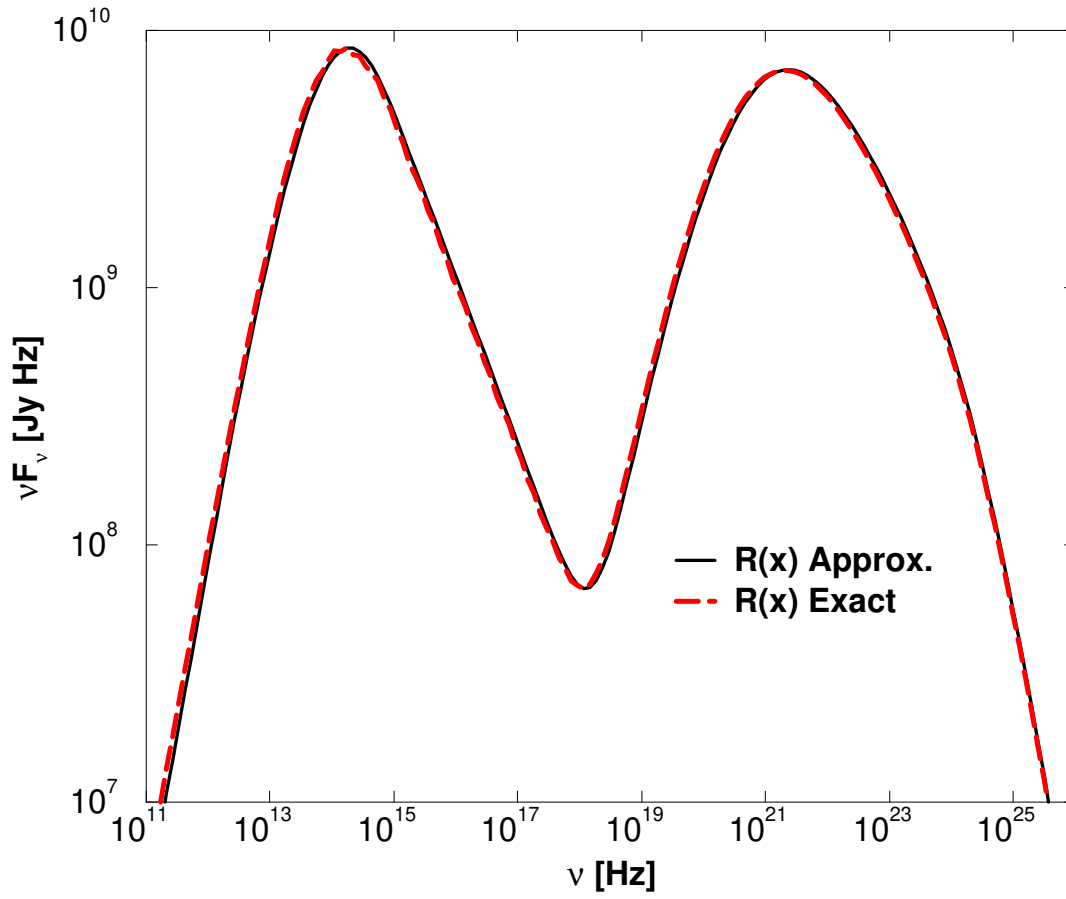


Fig. 14.— Comparison of the exact expression and numerical approximation of $R(x)$. The fit is accurate to $\sim 0.5\%$ for the entire frequency range.